Potential of ^{14}C-based versus ΔCO-based $\Delta ffCO_2$ observations to estimate urban fossil fuel CO_2 ($ffCO_2$) emissions

Fabian Maier[1], Christian Rödenbeck[2], Ingeborg Levin[1], Christoph Gerbig[2], Maksym Gachkivskyi[1,3], and Samuel Hammer[1,3]

[1]Institut für Umweltphysik, Heidelberg University, INF 229, 69120 Heidelberg, Germany
[2]Department of Biogeochemical Systems, Max Planck Institute for Biogeochemistry, Jena, Germany
[3]ICOS Central Radiocarbon Laboratory, Heidelberg University, Berliner Straße 53, 69120 Heidelberg, Germany

Correspondence to: Fabian Maier (Fabian.Maier@iup.uni-heidelberg.de)

Abstract. Atmospheric transport inversions are a powerful tool for independently estimating surface CO_2 fluxes from atmospheric CO_2 concentration measurements. However, additional tracers are needed to separate the fossil fuel CO_2 ($ffCO_2$) emissions from non-fossil CO_2 fluxes. In this study we focus on radiocarbon (^{14}C), the most direct tracer for $ffCO_2$, and the continuously measured surrogate tracer carbon monoxide (CO), which is co-emitted with $ffCO_2$ during incomplete combustion. In the companion paper by Maier et al. (2023a) we determined for the urban Heidelberg observation site in Southwestern Germany discrete ^{14}C-based and continuous ΔCO-based estimates of the $ffCO_2$ excess concentration ($\Delta ffCO_2$) compared to a clean-air reference. The ΔCO-based $\Delta ffCO_2$ concentration was calculated by dividing the continuously measured ΔCO excess concentration by an average ^{14}C-based $\Delta CO/\Delta ffCO_2$ ratio. Here, we use the CarboScope inversion framework adapted for the urban domain around Heidelberg to assess the potential of both types of $\Delta ffCO_2$ observations to investigate $ffCO_2$ emissions and their seasonal cycle. We find that although more precise ^{14}C-based $\Delta ffCO_2$ observations from almost 100 afternoon flask samples collected in the two years 2019 and 2020 are not well suited for estimating robust $ffCO_2$ emissions in the main footprint of this urban area with a very heterogeneous distribution of sources including several point sources. The benefit of the continuous ΔCO-based $\Delta ffCO_2$ estimates is that they can be averaged to reduce the impact of individual hours with an inadequate model performance. We show that the weekly averaged ΔCO-based $\Delta ffCO_2$ observations allow for a robust reconstruction of the seasonal cycle of the area source $ffCO_2$ emissions from temporally flat a-priori emissions. In particular, the distinct COVID-19 signal with a steep drop in emissions in spring 2020 is clearly present in these data-driven a-posteriori results. Moreover, our top-down results show a shift in the seasonality of the area source $ffCO_2$ emissions around Heidelberg in 2019 compared to the bottom-up estimates from the Netherlands Organization for Applied Scientific Research (TNO). This highlights the huge potential of ΔCO-based $\Delta ffCO_2$ to validate bottom-up $ffCO_2$ emissions at urban stations if the $\Delta CO/\Delta ffCO_2$ ratios can be determined without biases.

1 Introduction

The combustion of fossil fuels (ff) like coal, oil and gas is the major reason for the ongoing increase in the atmospheric CO_2 concentration, which causes current global warming. About 70% of the global $ffCO_2$ emissions are released from urban hotspot regions (Duren and Miller, 2012). Fortunately, the atmospheric CO_2 increase is weakened, since about half of the human-induced CO_2 emissions are currently taken up by the terrestrial biosphere and the oceans in roughly equal shares (Friedlingstein et al., 2022). Indeed, there are large seasonal and inter-annual variations in the non-fossil CO_2 sinks and sources that need to be better understood in order to make predictions about future changes in the carbon cycle owing to increased atmospheric CO_2 levels.

The "atmospheric transport inversion" (Newsam and Enting, 1988) is a powerful tool for deducing surface CO_2 fluxes from atmospheric CO_2 observations. Hence, many studies have applied this top-down approach to constrain CO_2 fluxes from terrestrial ecosystems and the oceans (e.g., Rödenbeck et al., 2003; Peylin et al., 2013; Jiang et al., 2016; Rödenbeck et al., 2018; Monteil et al., 2020; Liu et al., 2021). In these calculations, $ffCO_2$ emissions are typically prescribed using bottom-up information from emission inventories. These bottom-up $ffCO_2$ emission estimates are sometimes based on national annual activity data that describe the fuel consumption and sector-specific emission factors (Janssens-Maenhout et al., 2019). While annual national total $ffCO_2$ emissions are associated with low uncertainties of typically a few percent for developed countries (Andres et al., 2012), their proxy-based distribution on individual spatial grid cells and individual months, days or hours can dramatically increase the uncertainties (Peylin et al., 2013; Super et al., 2020). On the path to net zero emissions, independent verification of the reported national CO_2 emissions is essential. This includes the evaluation of the bottom-up statistics, especially on the relevant urban scales where uncertainties are larger and the most important emission reduction measures are implemented. Furthermore, the seasonal cycle of bottom-up $ffCO_2$ emissions needs to be validated, if they are used in CO_2 inversions to deduce biogenic CO_2 fluxes that are dominated by a large seasonal cycle.

Atmospheric transport inversions can be used to validate these bottom-up $ffCO_2$ emissions (e.g., Graven et al., 2018; Basu et al., 2020). However, their success relies on the ability of the used observational tracers to separate fossil fuel from non-fossil CO_2 contributions (Shiga et al., 2014; Ciais et al., 2015; Basu et al., 2016; Bergamaschi et al., 2018). The most direct tracer for $ffCO_2$ is radiocarbon (^{14}C) in CO_2. Radiocarbon has a half-life of 5700 years and is therefore no longer present in fossil fuels (Suess, 1955). Thus, the ^{14}C depletion in ambient air CO_2 compared to a clean-air reference site can directly be used to estimate the recently added $ffCO_2$ excess ($\Delta ffCO_2$) at the observation site (Levin et al., 2003; Turnbull et al., 2006). These $\Delta ffCO_2$ estimates can then be implemented in regional inversions to evaluate bottom-up $ffCO_2$ emissions in the footprints of the observation sites (Graven et al., 2018; Wang et al., 2018). However, a drawback of ^{14}C-based $\Delta ffCO_2$ estimates is that they have poor temporal and spatial coverage due to the labor-intensive and expensive ^{14}C sampling and analysis. Therefore, continuously measured atmospheric excess concentrations of trace gases like CO, which is co-emitted with $ffCO_2$, have been

used as alternative proxies for $\Delta ffCO_2$ (e.g., Gamnitzer et al., 2006; Turnbull et al., 2006; Levin and Karstens, 2007; van der Laan et al., 2010; Vogel et al., 2010). However, to construct a high-resolution ΔCO-based $\Delta ffCO_2$ record requires to correctly determine the $\Delta CO/\Delta ffCO_2$ ratio in the footprint of the observation site. This can indeed be a big challenge: As the $CO/ffCO_2$ emission ratio depends on the combustion efficiency and applied end-of-pipe measures, it is very variable for different emission processes and changes with time due to technological progress (Dellaert et al., 2019).

In the companion paper by Maier et al. (2023a) we calculated a ΔCO-based $\Delta ffCO_2$ record for the urban Heidelberg observation site by dividing the continuous ΔCO record from Heidelberg by an average $\Delta CO/\Delta ffCO_2$ ratio derived from almost 350 $^{14}CO_2$ flask samples collected between 2019 and 2020. We refer to this continuous $\Delta ffCO_2$ record as "ΔCO-based $\Delta ffCO_2$" in the following but emphasize that also here we used $^{14}CO_2$ flask observations to estimate the ΔCO-based $\Delta ffCO_2$. By comparing the hourly ΔCO-based $\Delta ffCO_2$ with the direct ^{14}C-based $\Delta ffCO_2$ from the flasks we estimated an uncertainty for these data of about 4 ppm, which is almost 4 times larger than typical ^{14}C-based $\Delta ffCO_2$ uncertainties. About half of this uncertainty could be attributed to the spatiotemporal variability of the $\Delta CO/\Delta ffCO_2$ ratios (Maier et al., 2023a).

The goal of this study is to investigate which type of $\Delta ffCO_2$ observations provides the greater benefit in an atmospheric transport inversion to validate bottom-up $ffCO_2$ emission estimates in an urban region: (1) sparse ^{14}C-based $\Delta ffCO_2$ observations from flasks with a small uncertainty or (2) ΔCO-based $\Delta ffCO_2$ estimates at high temporal resolution but with an increased uncertainty? For this, we adapt the CarboScope inversion framework (Rödenbeck, 2005) for the highly populated and industrialized Rhine Valley in Southwestern Germany around the Heidelberg observation site. We perform separate inversion runs with the ^{14}C- and ΔCO-based $\Delta ffCO_2$ observations from Heidelberg. Thereby, we mainly focus on the seasonal cycle in the $ffCO_2$ emissions and investigate which $\Delta ffCO_2$ information leads to robust inversion results and is thus best suited to validate the seasonal cycle of the bottom-up emissions in the main footprint of Heidelberg.

2 Methods

2.1 Heidelberg observation site

Heidelberg is a medium-sized city with about 160'000 inhabitants, which is part of the Rhine-Neckar metropolitan area with over 2 million people. The Heidelberg observation site is located on the university campus in the north-western part of the city. The sampling inlet line is 30 m above ground on the roof of the institute's building. Local $ffCO_2$ emissions originate mainly from traffic and residential heating but there is also a nearby combined heat and power station as well as a large coal-fired power plant and the giant industrial complex from BASF 15-20 km to the North-West. Due to its location in the Upper Rhine Valley, Heidelberg is frequently influenced by south-westerly air masses, which carry the signals from heterogeneous sources in the Rhine Valley. A more detailed description of the Heidelberg observation site can be found in Levin et al. (2011). The ^{14}C-based and ΔCO-based $\Delta ffCO_2$ observations from Heidelberg are presented in Sect. 2.2.3.

2.2 Inversion setup

The CarboScope inversion algorithm was initially introduced by Rödenbeck et al. (2003) to estimate inter-annual and spatial variability in global CO_2 surface-atmosphere fluxes. The algorithm can also be applied to regional inversions (Rödenbeck et al., 2009). In the present study we adapt this inversion modelling framework to estimate $ffCO_2$ surface fluxes in the regional Rhine Valley domain (see Fig. 1) with $\Delta ffCO_2$ observations from the Heidelberg observation site (see Fig. 2). This requires a high-resolution atmospheric transport model and a careful estimation of the lateral $\Delta ffCO_2$ boundary conditions.

The CarboScope inversion system uses Bayesian inference to minimize the deviations between observed and modelled $\Delta ffCO_2$ concentrations by finding the (global) minimum of the cost function (for technical details see Appendix A and Rödenbeck, 2005). This cost function consists of a data constraint and an a-priori flux constraint, which is needed to regularize the underdetermined problem and to prevent large and unrealistic spatiotemporal $ffCO_2$ flux variabilities (Rödenbeck et al., 2018). The data constraint is weighted by the uncertainties of the transport model and the $\Delta ffCO_2$ observations. Furthermore, the uncertainty applied for the a-priori $ffCO_2$ emissions determines the impact of the a-priori constraint. Overall, the ratio between the model-data uncertainty and the a-priori flux uncertainty controls the strength of the a-priori constraint over the observational constraint (Rödenbeck, 2005; Kountouris et al., 2018; Munassar et al., 2022). The cost function is minimized by using a conjugate gradient algorithm with reorthogonalization after each iteration step (Rödenbeck, 2005). In this study we optimize every day a single scalar on the a-priori $ffCO_2$ emissions field inside the Rhine Valley domain.

2.2.1 Atmospheric transport model

We use the Stochastic Time-Inverted Lagrangian Transport (STILT; Lin et al., 2003; Nehrkorn et al., 2010) model, driven by meteorological fields from the high-resolution Weather Research and Forecasting model (WRF, version 3.9.1.1, Skamarock et al., 2008), to simulate the atmospheric transport in the Rhine Valley domain (see red rectangular in Fig. 1). Hourly 0.25°-resolved European ReAnalysis 5 (ERA5, Hersbach et al., 2020) data from the European Centre for Medium-Range Weather Forecasts (ECMWF) were used as boundary conditions for the WRF simulations. The WRF meteorological fields have a horizontal resolution of 2 km and were generated by applying the MYNN (Mellor-Yamada Nakanishi Niino, Nakanishi and Niino, 2009) planetary boundary layer (PBL) parameterization scheme. Finally, we calculated with STILT the sensitivity of the Heidelberg observations to $ffCO_2$ emissions from individual grid cells in the catchment area of the site (i.e. the so-called footprint in units of concentration per flux density) by computing for each hour the back-trajectories of 100 particles released from the Heidelberg receptor site. The hourly-resolved footprints have a horizontal resolution of about 1 km x 1 km (1/60° x 1/120°, lon. x lat.). As there are many point source emissions within the Rhine Valley, we apply the STILT volume source influence (VSI) approach introduced by Maier et al. (2022) to model them. This model approach takes into account the effective heights (including plume rise) of the point source emissions, which are typically released from elevated chimney stacks. This approach substantially improved the simulation of $\Delta ffCO_2$ concentrations at the Heidelberg site, especially during situations

with low PBL heights (Maier et al., 2022). For the area source emissions, we apply the standard approach in STILT, which assumes that all emissions are released from the surface.

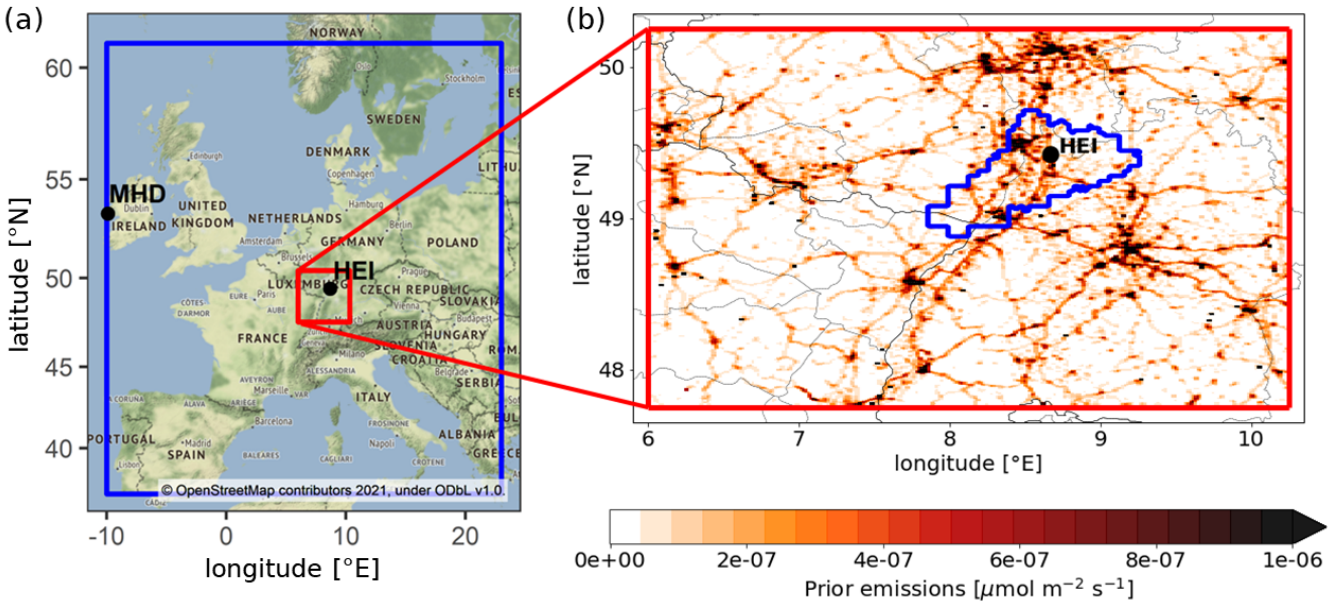

Figure 1: (a) Map with the Central European STILT domain (blue) and the high-resolution Rhine Valley STILT domain (red). The observation site Heidelberg (HEI) and the marine site Mace Head (MHD), which we used as a background site to calculate the $\Delta ffCO_2$ concentrations at Heidelberg (see Sect. 2.2.3), are indicated. (b) Zoom into the Rhine Valley domain with the mean prior $ffCO_2$ emissions from the TNO inventory for 2019-2020. The blue outline in the zoom shows the "50%-footprint" range, i.e., the area accounting for 50% of the Heidelberg average footprint within the Rhine Valley.

2.2.2 A-priori information

We use the $ffCO_2$ emissions from the Netherlands Organization for Applied Scientific Research (TNO, Dellaert et al., 2019; Denier van der Gon et al., 2019) with a horizontal resolution of about 1 km (1/60° lon. x 1/120° lat.) as a-priori estimates for our Rhine Valley inversion. The TNO emission inventory provides annual $ffCO_2$ emissions for 15 different source sectors as well as sector-specific temporal profiles. In this study, we treat the $ffCO_2$ emissions from the point source dominated "energy production" and "industry" TNO sectors separately due to the following reasons: (1) While the VSI approach (see above) strongly improves the vertical representation of point source emissions in STILT (Maier et al., 2022), it still remains difficult to correctly describe the mixing and transport of narrow point source plumes with meteorological fields that have a resolution of 2 km. (2) Due to the elevated release of point source emissions from high stacks, the Heidelberg observation site with an air intake height of only 30 m above ground is rarely influenced by distinct emission plumes from nearby point sources (see Fig. 4 with the $\Delta CO/\Delta ffCO_2$ ratio analysis in Maier et al., 2023a). This makes it difficult to evaluate those point source emissions with $\Delta ffCO_2$ observations from the Heidelberg observation site alone. (3) As the energy and industry point source emissions in TNO are directly based on the European Pollutant and Transfer Register (E-PRTR) database, which provides

information on the location and emission of the major facilities in Europe (Kuenen et al., 2014), we expect them to be better known than the more diffuse area source emissions in the Rhine Valley. We thus focus on how well our observations are able to constrain area source emissions in the footprint of the Heidelberg site.

We, thus, prescribe the energy and industry emissions in our inversion setup and adjust only the area source emissions in the Rhine Valley, which mainly originate from the heating and traffic sector. TNO provides monthly profiles for the $ffCO_2$ emissions from each of the 15 source sectors. We use the monthly profiles for 2019, which are European averages and thus identical for all countries within the Central European STILT domain (see blue box in Fig. 1a). For 2020 TNO provides country-specific temporal profiles to account for the large variabilities in length and intensity of the COVID-19 restrictions among the individual countries. As Germany and France are both part of the Rhine Valley domain, we decided to use the average of the German and French temporal profiles for 2020 to construct suitable sector-specific monthly profiles for the Rhine Valley domain in 2020. For all inversion runs performed in this study, we use these TNO monthly profiles to calculate from the corresponding annual total emissions monthly $ffCO_2$ emissions for the energy and industry sectors.

In this study, we aim to evaluate the information of the $\Delta ffCO_2$ observations regarding the seasonal cycle of the area source $ffCO_2$ emissions. That is why we apply in our standard inversion runs temporally constant ("flat") a-priori $ffCO_2$ emissions for the area sources. For this, we use the (spatially highly resolved) 2-year average TNO area source emissions of the years 2019 and 2020. Finally, we also perform a sensitivity inversion run, for which we replace the temporally flat a-priori area source emissions by monthly varying a-priori area source emissions. For this, we use for both, the area and the point source emissions, the monthly profiles from TNO described above (i.e., the European average monthly profiles in 2019 and the mean of the German and French monthly profiles in 2020).

2.2.3 Observations

In separate inversion runs, we use either the discrete ^{14}C-based $\Delta ffCO_2$ estimates from flasks, collected as integrals over one hour, or the hourly ΔCO-based $\Delta ffCO_2$ record from the Heidelberg observation site (see Fig. 2). The companion paper (Maier et al., 2023a) describes in detail the calculation of the ^{14}C-based $\Delta ffCO_2$ estimates as well as the construction of the continuous ΔCO-based $\Delta ffCO_2$ record. In short, the ΔCO-based $\Delta ffCO_2$ record has been constructed by dividing the continuously measured hourly ΔCO offsets compared to the marine reference site Mace Head (MHD) by an average $\Delta CO/\Delta ffCO_2$ ratio of 8.44±0.07 ppb/ppm, which was determined from ΔCO and ^{14}C-based $\Delta ffCO_2$ observations of almost 350 day- and night-time flask samples collected in 2019 and 2020. Correlation of these ΔCO and $\Delta ffCO_2$ values showed only small variability, because heating and traffic $CO/ffCO_2$ emission ratios in the footprint of Heidelberg are currently very similar around 8 ppb/ppm. In the inversion, however, we only use the afternoon ^{14}C-based and ΔCO-based $\Delta ffCO_2$ observations between 11 and 16 UTC, as night-time situations are associated with a poorer transport model performance. Times for the hourly-integrated $\Delta ffCO_2$ observations are reported as the start of the hour, e.g. 11 UTC corresponds to the time period between 11 and 12 UTC. The

average uncertainties of the ^{14}C- and ΔCO-based $\Delta ffCO_2$ concentrations were estimated to 1.1 ppm and 3.9 ppm, respectively (Maier et al. 2023a,b)

Furthermore, we apply a 2σ-selection criterion to the $\Delta ffCO_2$ observations as introduced by Rödenbeck et al. (2018). For this, we take the high-resolution annual total $ffCO_2$ emissions from TNO and apply the hourly sector-specific temporal profiles. These hourly resolved $ffCO_2$ emissions are then transported with the WRF-STILT model to simulate hourly $\Delta ffCO_2$ concentrations. The mean difference between the simulated and the ΔCO-based $\Delta ffCO_2$ observations is only -0.04 ppm during afternoon hours with a standard deviation of 6.76 ppm (i.e., almost 100% of the mean value), which indicates that the model is able to reproduce, on average, the afternoon ΔCO-based $\Delta ffCO_2$ observations without a significant mean bias. This directly allows the application of the 2σ-selection criterion, which means that we only use those $\Delta ffCO_2$ observations, whose deviation to the modelled $\Delta ffCO_2$ is smaller than 2 times the standard deviation between observed and modelled $\Delta ffCO_2$, i.e. which is within the 2σ-range. Therewith, we exclude the data outside the 2σ-range, which obviously cannot be represented with our transport model. Examples of such data are observations during very strong air stagnation events in winter, which are often underestimated in the model, or vice versa, situations when the model overestimates the point source influence at the observation site. Since the inversion system assumes a Gaussian distribution for the model-data mismatch, these extreme outlier events would have a strong impact on the inversion results (Rödenbeck et al., 2018). Thus, this 2σ-selection can be seen as an additional regularization for the inversion to avoid using situations with unrealistic model simulations. We apply the 2σ-selection criterion to both the ^{14}C-based $\Delta ffCO_2$ observations from the afternoon flask samples and the afternoon hours of the ΔCO-based $\Delta ffCO_2$ record.

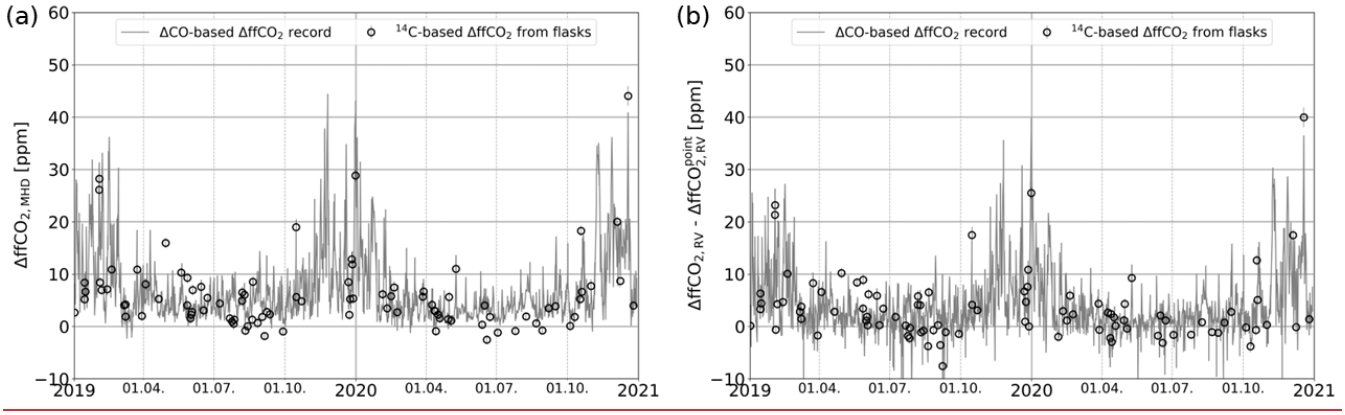

Figure 2: Afternoon $\Delta ffCO_2$ observations from the Heidelberg observation site. The grey curve indicates the ΔCO-based $\Delta ffCO_2$ record and the black circles the ^{14}C-based $\Delta ffCO_2$ estimates from flasks. Both, the ^{14}C-based and ΔCO-based $\Delta ffCO_2$ observations are 2σ-selected. (a) shows the $\Delta ffCO_2$ excess compared to the marine background site Mace Head (i.e. $\Delta ffCO_{2,MHD}$ in Eq. 1). (b) shows the $\Delta ffCO_2$ excess compared to the Rhine Valley (RV) boundary (i.e. $\Delta ffCO_{2,RV}$ in Eq. 1) *minus* the modelled $\Delta ffCO_{2,RV}$ contributions from point sources within the Rhine Valley ($\Delta ffCO^{point}_{2,RV}$). The data in (b) are effectively used to optimize the area source emissions in the Rhine Valley.

2.2.4 Lateral boundary conditions

We set up the inversion system for the Rhine Valley domain (6.00°E – 10.25°E, 47.75°N – 50.25°N, red rectangular in Fig. 1a) around the Heidelberg observation site and run the inversion for the full two years 2019 and 2020 within this domain. However, as we calculated the ^{14}C- and ΔCO-based $\Delta ffCO_2$ excess compared to MHD (see Maier et al., 2023a), we need to define a suitable $\Delta ffCO_2$ background representative for the boundary of the Rhine Valley domain. In the following, we call this the "Rhine Valley $\Delta ffCO_2$ background". By definition, we assume that the $\Delta^{14}CO_2$ observations from MHD correspond to $\Delta ffCO_2 = 0$ ppm, which is reasonable since the MHD $^{14}CO_2$ samples were only collected during situations with clean westerly air masses from the Atlantic. Therefore, it seems to be suitable to apply the MHD ($\Delta ffCO_2 = 0$ ppm) background to the entire western boundary of the Central European STILT domain (blue rectangular in Fig. 1a). But how representative is this background for the other boundaries of the Central European domain? Maier et al. (2023b) estimated the representativeness bias of the MHD background for the eastern boundary of the Central European domain, which is likely the most polluted border. They showed that the representativeness bias is on average smaller than 0.1 ppm for an observation site in Central Europe. Therefore, we neglect this bias and assume $\Delta ffCO_2 = 0$ ppm also at the non-western boundaries of the Central European domain. To estimate the Rhine Valley $\Delta ffCO_2$ background we then use a nested STILT model approach with 2 km horizontal resolution WRF meteorology in the Rhine Valley domain and coarser (10 km) WRF resolution in the Central European STILT domain *outside* the Rhine Valley. For both domains we use hourly $ffCO_2$ emissions from TNO (Dellaert et al., 2019; Denier van der Gon et al., 2019). This nested approach allows us to separate the $ffCO_2$ contributions from each STILT domain. With this setup we model for the Heidelberg site for each hour during 2019 and 2020 the $\Delta ffCO_2$ contributions from the Central European domain *outside* the Rhine Valley ($\Delta ffCO_{2,CE\text{-}RV}$), which we use as the Rhine Valley background. We then subtract this modelled Rhine Valley $\Delta ffCO_2$ background ($\Delta ffCO_{2,CE\text{-}RV}$) from the estimated $\Delta ffCO_2$ excess compared to MHD ($\Delta ffCO_{2,MHD}$), to obtain the $\Delta ffCO_2$ excess compared to the Rhine Valley boundary ($\Delta ffCO_{2,RV}$):

$$\Delta ffCO_{2,RV} = \Delta ffCO_{2,MHD} - \Delta ffCO_{2,CE\text{-}RV} \quad (1)$$

The $\Delta ffCO_{2,RV}$ excess concentrations compared to the Rhine Valley boundary are then introduced into the inversion system to constrain the $ffCO_2$ emissions within the Rhine Valley. Note, however, that the actual data constraint is the $\Delta ffCO_{2,RV}$ excess *minus* the modelled $\Delta ffCO_2$ contribution from the point sources within the Rhine Valley ($\Delta ffCO_{2,RV}^{point}$, see Fig. 2b), since we prescribe the point source emissions and only optimize for the area source emissions.

We also want to emphasize that the $\Delta ffCO_{2,RV}$ excess concentrations rely on the STILT transport and the TNO emissions to be correct. A potential bias in the modelled transport or the $ffCO_2$ emissions outside the Rhine Valley would directly translate into a bias in the $\Delta ffCO_{2,RV}$ excess concentrations. This in turn might affect the deduced $ffCO_2$ fluxes within the Rhine Valley domain. To assess the impact of the Rhine Valley $\Delta ffCO_2$ background ($\Delta ffCO_{2,CE\text{-}RV}$) on the a-posteriori $ffCO_2$ fluxes in the main footprint of Heidelberg, we also perform an inversion run with an alternative Rhine Valley $\Delta ffCO_2$ background. We again model this alternative background with STILT but apply the 0.25°-resolved forecasting meteorological data from the

Integrated Forecasting System (IFS) instead of the WRF meteorology (see Sect. 2.2.1). Moreover, we replace the TNO emissions by the Emissions Database for Global Atmospheric Research (EDGAR, version 4.3.2, Janssens-Maenhout et al., 2019) emissions to prescribe the $ffCO_2$ fluxes in Europe. This EDGAR inventory was updated to the years 2019 and 2020 by taking into account the British Petroleum (BP) statistics on fossil fuel consumptions and was remapped on a grid with a horizontal resolution of 0.25°. Note, that we only use this coarser STILT resolution for simulating the alternative Rhine Valley $\Delta ffCO_2$ background. The inversion itself is again performed with the high resolution WRF meteorology (see Sect. 3.3).

2.2.5 Model-data mismatch

The model-data mismatch (MDM) is calculated by subtracting the modelled from the observed $\Delta ffCO_{2,RV}$ concentrations. The uncertainties of the ΔCO-based and ^{14}C-based $\Delta ffCO_2$ observations are estimated to be 3.9 ppm and 1.1 ppm, respectively (see Maier et al., 2023a). The transport model uncertainty of urban, continental sites like Heidelberg with complex local circulations was assumed to be 5 ppm. The quadratically added observational and transport model uncertainties yield the total uncertainty of the model-data mismatch, which we call the MDM error in the following. To account for the temporal correlations of observations that are close together in time, we apply a data density weighting as described in Rödenbeck (2005). It artificially increases the MDM error, so that all observations within one week lead to the same constraint as a single observation per week. The weighting interval was set to one week because this is a typical duration of synoptic weather patterns. Depending on the number of observations per week, the final MDM error of individual hourly observations ranges between 5.1 and 7.8 ppm in the case of ^{14}C-based $\Delta ffCO_2$ from flasks and between 23.7 and 37.5 ppm in the case of the ΔCO-based $\Delta ffCO_2$ record.

Based on our analysis results presented in Sect. 3.1, we decided to apply a weekly averaging in the case of the ΔCO-based $\Delta ffCO_2$ inversion (see Sect. 3.2), which we briefly describe here. The MDM vector for the ΔCO-based $\Delta ffCO_2$ inversion has a length of 3237, which represents the number of the (2σ-selected) afternoon hours with available ΔCO-based $\Delta ffCO_2$ observations. Weekly averaging means that each hourly entry of the MDM vector within a week is replaced by the respective *weighted* average MDM of that week. The weight of the individual hours within a week is defined by the MDM error of the respective hours. This means that the weekly averaged MDM vector has the same length as the original MDM vector. We do not modify the hourly MDM errors when applying the weekly averaging. This means that the weekly averaging would not change anything if all hourly MDM entries within a week were initially (by chance) the same.

2.2.6 Degrees of freedom

Since we only use $\Delta ffCO_2$ observations from one single station in the Rhine Valley, we restrict the number of degrees of freedom in our inversion system so that the inverse problem is not too strongly underdetermined. Therefore, we only investigate the area source emissions in the Rhine Valley and prescribe the energy and industry emissions, as described above. Moreover, the inversion system adjusts only one spatial scaling factor per day, which increases or decreases the area source emissions in

the whole Rhine Valley domain equally. Hence, we expect that the high-resolution TNO inventory is much better at describing the large spatial heterogeneity in the $ffCO_2$ emissions within the Rhine Valley than our top-down approach. As we want to investigate the seasonal cycle of the $ffCO_2$ emissions, additional temporal degrees of freedom are needed. For this, we choose a temporal correlation length of about 4 months ("Filt3T" in CarboScope notation), which should be appropriate to explore seasonal cycles. Finally, since the Heidelberg observations cannot be used to constrain the emissions in the whole Rhine-Valley domain, we only analyze the a-posteriori area source emissions in the (most constrained) nearfield of the observation site. We define the nearfield of Heidelberg as the area which accounts for 50% of the temporally accumulated footprint in the Rhine Valley domain for the two years 2019 and 2020 (blue surrounded region in Fig. 1b).

3 Results

3.1 Potential of flask-based ΔffCO$_2$ estimates to investigate the seasonal cycle in ffCO$_2$ emissions

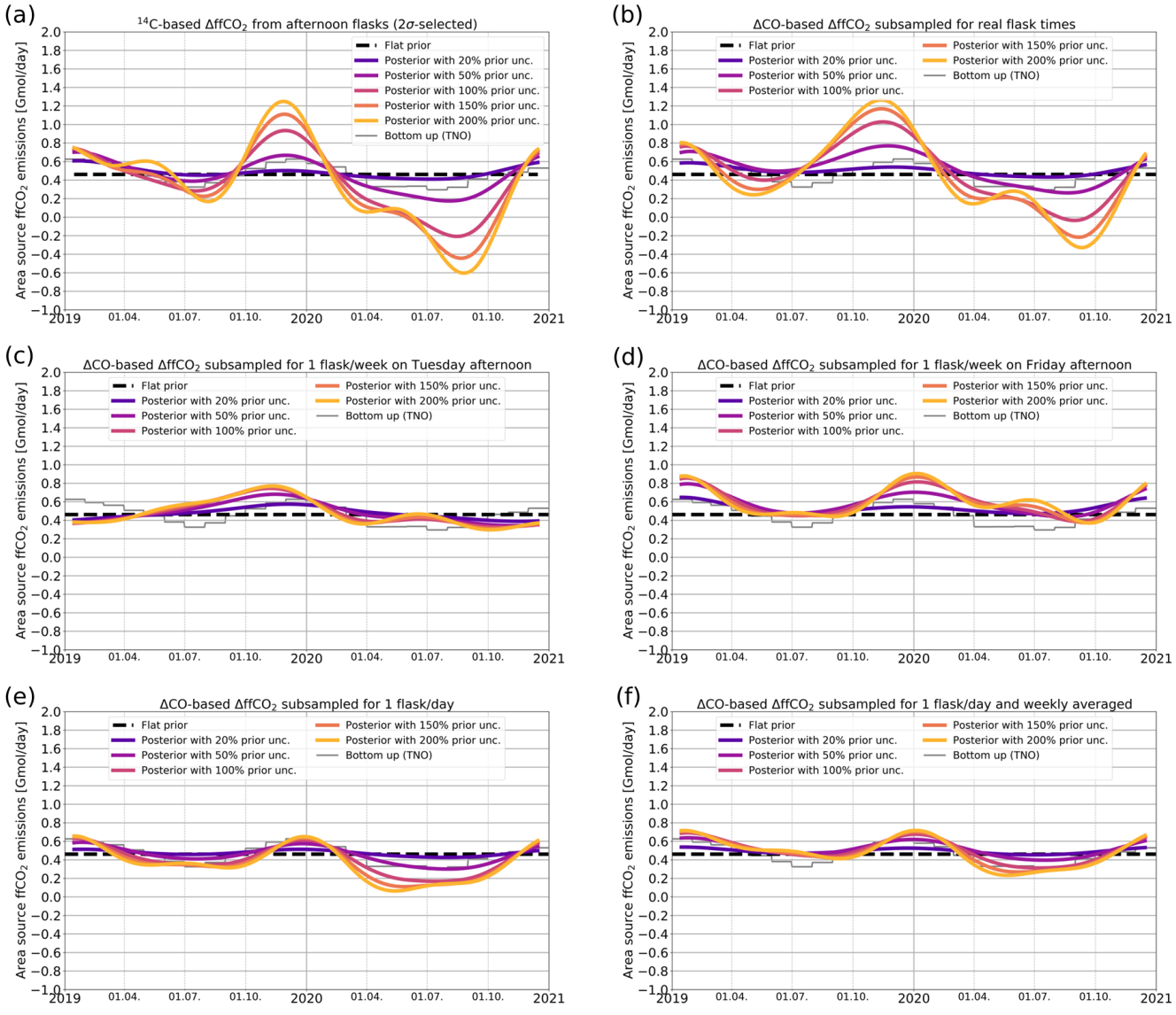

Figure 3: Area source ffCO$_2$ emissions in the nearfield (blue outlined area in Fig. 1b) of Heidelberg. Shown are the flat prior emissions (black dashed line), the a-posteriori emissions for different prior uncertainties between 20% and 200% of the flat a-priori emissions (colored solid lines) as well as the bottom-up estimates from TNO (grey line). In panel (a) ^{14}C-based ΔffCO$_2$ estimates from 94 2σ-selected afternoon flasks from Heidelberg were used as observational input (cf. Fig. 2). Panel (b) shows the inversion results if the ΔCO-based ΔffCO$_2$ observations subsampled during the 94 flask sampling hours were used. In the panels (c) and (d) the inversion was constrained with one hourly afternoon (at 13 UTC) ΔCO-based ΔffCO$_2$ observation every week collected on the two random working days Tuesday (c) or Friday (d). Panel (e) shows the results if each day at 13 UTC one hypothetical flask is collected. In panel (f), the 7 afternoon flask observations within one week are averaged.

First, we investigate the potential of flask-based $\Delta ffCO_2$ estimates to resolve the seasonal cycle of the area source $ffCO_2$ emissions around the urban Heidelberg observation site. For this we use the average of the TNO area source $ffCO_2$ emissions of the two years 2019 and 2020 as a temporally constant prior estimate (see Sect. 2.2.2). To analyze the impact of the observational constraint on the a-posteriori results, we apply different prior uncertainties, which effectively lead to different ratios between a-priori and data constraint (Fig. 3). In a first inversion run (Fig. 3a), we use the ^{14}C-based $\Delta ffCO_2$ observations from the 94 afternoon flasks collected in the two years 2019 and 2020 in Heidelberg. The distribution of the flask samplings over the two years can be seen in Fig. 2. Due to various reasons (e.g. testing of the flask sampler associated with frequent changes of the flask sampling strategy) the flasks were not evenly collected and especially the winter 2019/2020 has only limited flask coverage. The ^{14}C-based a-posteriori $ffCO_2$ emissions show a clear seasonal cycle for the larger prior uncertainties, which is mainly data-driven. However, large and unrealistic a-posteriori flux variabilities emerge for prior uncertainties larger than 50% of the flat a-priori emissions. For example, the low flask coverage during the winter period 2019/2020 leads to a huge maximum in the area source $ffCO_2$ emissions in November 2019 when the inversion algorithm tries to fit individual flask observations that have large model-data mismatches (see Fig. B1). Similarly, the flask samples in summer 2020 with near-zero or even negative $\Delta ffCO_2$ estimates, which lead to negative model-data mismatches (cf. Fig. 2b and Fig. B1) cause a strong reduction of the a-posteriori emissions.

Fig. B1 shows the agreement between the flat prior and the different a-posteriori-based model results and the flask observations. The flat prior emissions lead to a mean bias (observed minus modelled $\Delta ffCO_2$ concentration) of 0.68 ppm with a standard deviation of 5.61 ppm. The a-posteriori emissions based on a 50% prior uncertainty reduces the mean bias and the standard deviation to 0.35 ± 5.23 ppm. However, for higher prior uncertainties, the mean bias increases again and only the standard deviation is further reduced; e.g. a prior uncertainty of 150% leads to a mean bias of 0.54 ± 4.78 ppm between observed and modelled $\Delta ffCO_2$ concentration. This might be an indication for overfitting. To further investigate the performance of the inversion, we conducted a reduced chi-squared (χ_r^2) analysis. The χ_r^2 values decrease from 1.10 (for a 50% prior uncertainty) to 0.97 (150% prior uncertainty). Typically, χ_r^2 values smaller than 1 are an indication for overfitting if the model-data mismatch error is chosen properly. However, as the χ_r^2 values (for prior uncertainties between 50 and 200%) are all close to 1 (within ±10%), the χ_r^2 values might not be suitable to demonstrate overfitting in our case. Overall, this urban inversion setup obviously needs a very strong regularization through low prior uncertainties to prevent fitting of individual flask observations and thus unrealistic variability in the a-posteriori $ffCO_2$ emissions. This indicates that the applied 2σ-filtering approach (see Sect. 2.2.3) is not sufficient in this urban setting.

We further investigate whether these overfitting patterns can be attributed to the uneven distribution of the flask samples. For this, we subsample the continuous ΔCO-based $\Delta ffCO_2$ record. In a first step, we use the ΔCO-based $\Delta ffCO_2$ observations from those 94 afternoon hours with flask samplings as observational constraint (Fig. 3b). For the most part, the subsampled ΔCO-based $\Delta ffCO_2$ observations reproduce the a-posteriori results of the ^{14}C-based $\Delta ffCO_2$ estimates. However, there are differences

like the shifted summer minimum in 2019. These differences can be explained by the deviations between the ^{14}C-based and ΔCO-based $\Delta ffCO_2$ estimates in Fig. 2, and thus the variability of the $\Delta CO/\Delta ffCO_2$ ratios that we fully neglected by using a constant mean ratio for constructing the ΔCO-based $\Delta ffCO_2$ record. Thus, when comparing the results with the TNO seasonality of emissions (grey histogram) it seems obvious that the ^{14}C-based $\Delta ffCO_2$ estimates provide the more accurate data than the subsampled ΔCO-based $\Delta ffCO_2$ record. However, the general similarity between both results means that we can use the continuous ΔCO-based $\Delta ffCO_2$ record to investigate an even data coverage with hypothetical Heidelberg flask samples. The middle panels in Fig. 3 show the inversion results if the ΔCO-based $\Delta ffCO_2$ record is subsampled for one flask every week on Tuesday (c) or on Friday afternoon (d), respectively. We chose Tuesday and Friday as random examples for two working days. The evenly distributed weekly flasks strongly dampen the variability of the a-posteriori results. However, they show large differences depending on which day of the week the hypothetical afternoon flask was collected. Whereas the Tuesday flasks lead to a quite unrealistic gradual increase in the $ffCO_2$ emissions between January and November 2019, the Friday flasks show a more realistic seasonal cycle in this year. In contrast, both Tuesday and Friday flasks lead to an unexpected maximum in summer 2020. The comparison between the (hypothetical) flask concentrations and the a-posteriori results illustrates again that the inversion mainly tries to fit those individual hours with the largest MDM (not shown). This implies that the a-posteriori results are still dependent on the selection of the individual hypothetical flasks. Therefore, it seems that even a uniform data coverage with a realistic flask sampling frequency of one flask per week is not sufficient to determine a plausible seasonal cycle of the area source $ffCO_2$ emissions around Heidelberg (as e.g. suggested by the TNO inventory). However, the situation should be improved in the case of real, hourly-integrated ^{14}C flasks that are collected e.g. once per week, as the average $\Delta CO/\Delta ffCO_2$ ratio used to construct the ΔCO-based $\Delta ffCO_2$ record might be inappropriate for individual hours.

Finally, we investigated the benefit of an extremely high flask sampling frequency with one flask per afternoon (see Fig. 3e). Note, that such a high-frequent flask sampling increases the MDM error because of the applied data density weighting (see Sect. 2.2.5). Here, the a-posteriori results seem to approach towards the TNO bottom-up emissions in 2019. However, there are still unexpectedly strong deviations between the top-down and bottom-up estimates in the summer half-year 2020 for increased prior uncertainties. These differences might be caused by individual afternoon hours with a negative MDM in summer 2020. To reduce the impact of such hours, we perform a separate inversion run where we average the modelled and observational data of all 7 hypothetical afternoon flasks within each week (Fig. 3f, see Sect. 2.2.5 for a description of the weekly averaging of the MDM vector). This further reduces the spread of a-posteriori results, particularly in summer 2020, further approaching towards the seasonal amplitude of the bottom-up TNO emissions. Thus, several afternoon flasks per week would be needed so that the influence of individual flasks on the inversion results can be averaged out and a plausible seasonal cycle amplitude in the area source $ffCO_2$ emissions around Heidelberg can be obtained.

Overall, these results show that the a-posteriori estimates are very sensitive to individual flask observations in the Heidelberg target region with very heterogeneously distributed $ffCO_2$ sources. Obviously, the transport model fails to appropriately simulate the $\Delta ffCO_2$ concentrations for individual afternoon hours. This can be explained by remaining shortcomings in the transport model but also by the enormous heterogeneity of the $ffCO_2$ emissions in the footprint of the Heidelberg observation site. As already mentioned in Sect. 2, modelling individual plumes from point source emissions is a particular challenge in this urban region, and e.g. the forward model estimates of point source signals, even with the improved VSI approach seem often incorrect, at least at a temporal resolution of one hour. Moreover, there might also be inaccuracies in the TNO point source emissions themselves. Finally, part of the MDM can also be explained by uncertainties in the proxies used to spatially disaggregate the area source emissions in the TNO inventory (Super et al., 2020).

3.2 Potential of continuous ΔCO-based $\Delta ffCO_2$ estimates to investigate the seasonal cycle in $ffCO_2$ emissions

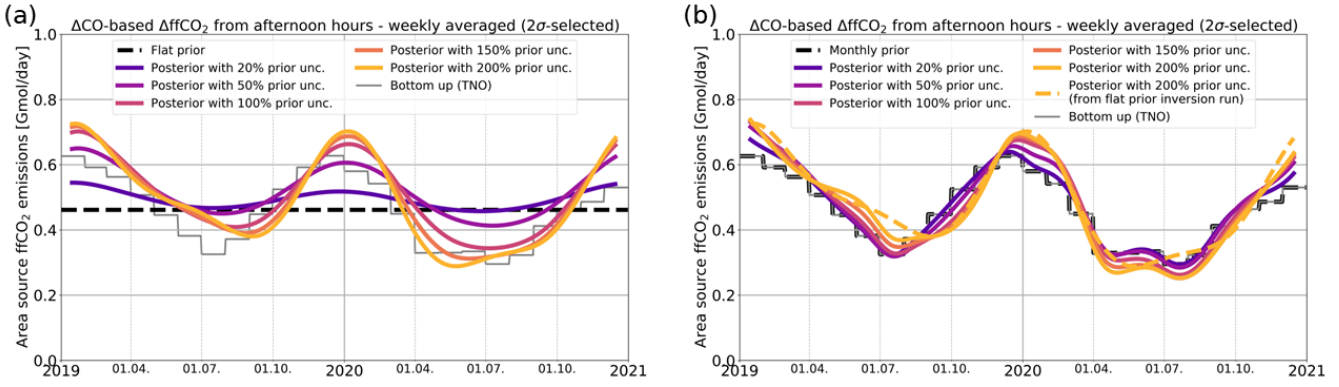

Figure 4: Area source $ffCO_2$ emissions in the nearfield (blue outlined area in Fig. 1b) of Heidelberg. In (a) a flat prior (black dashed line) was used for the area source emissions and in (b) a monthly prior, i.e. the monthly bottom-up estimates from TNO (grey dashed line) were used as a-priori estimate. Shown are the a-posteriori emissions for different prior uncertainties between 20 and 200% (colored solid lines). The inversion was constrained with weekly averages of hourly, 2σ-selected afternoon ΔCO-based $\Delta ffCO_2$ observations from Heidelberg. For comparison, the posterior emissions with 200% prior uncertainty from (a) are shown as a yellow dashed line in (b).

The big advantage of the continuous ΔCO-based $\Delta ffCO_2$ record is that it provides a full temporal coverage of the inversion period and can, thus, also be averaged such that the sensitivity of the a-posteriori results on individual (hourly) model-data mismatches with poor model performance is strongly reduced. In Appendix C, we investigate over which time interval the hourly ΔCO-based and modelled $\Delta ffCO_2$ concentrations should be averaged to sufficiently reduce the impact of the point source emissions on the a-posteriori area source emissions. For this, we perform in addition to the standard inversion runs with fixed point source emissions further sensitivity runs with adjustable point source emissions. Ideally (i.e. if the point source emissions are well described in TNO), the a-posteriori area source emissions are identical for both inversion runs, meaning that the modelling of the better known point source emissions has no impact on the area source emissions. It turns out that the averaging interval of one week strongly reduces the impact of the point sources on the a-posteriori area source emissions (see blue curves in Fig. C1). It limits the differences between the a-posteriori area source emissions of the inversion runs with fixed

and adjustable point source emissions to below 30% for individual seasons. Averaged over the two years 2019 and 2020, these differences are below 10%. For the ΔCO-based $\Delta ffCO_2$ inversion, we therefore apply a weekly averaging to the MDM vector (as described in Sect. 2.2.5).

In the following, we use the weekly averaged afternoon ΔCO-based $\Delta ffCO_2$ observations to investigate the seasonal cycle of the area source $ffCO_2$ emissions around Heidelberg (see Fig. 4a). If the prior uncertainty is chosen large enough, the seasonal cycle amplitude of the a-posteriori estimates agrees with that of the TNO inventory reasonably well. Moreover, the data-driven inversion results distinctly show the effect of the COVID-19 restrictions with lower emissions in 2020 compared to 2019. In Southwestern Germany, the first COVID-19 lockdown started in mid-March 2020. Indeed, the inversion results show at that time a strong decrease in the area source $ffCO_2$ emissions. In particular, the decline in the a-posteriori $ffCO_2$ emissions is much steeper in spring 2020 compared to spring 2019 and the minimum of the seasonal cycle is flatter in 2020 as it extends over several summer months. The sharp drop in emissions at the beginning of the COVID-19 restrictions in spring 2020 can also be seen in Fig. D1, where we plot the difference between the seasonal cycles of the two years.

The agreement with the phasing of the seasonal cycle of the TNO inventory seems to be better in 2020 than in 2019. As described in Sect. 2.2.2., TNO provides for 2020 country-specific "COVID-19" time profiles, which take into account the timing and the strength of the respective national restrictions. For this year, Fig. 4 shows the average of the monthly time profiles from Germany and France applied to the annual Rhine Valley emissions (grey histogram). This seasonal cycle for 2020 seems to be confirmed by our observations. However, the TNO seasonal cycle shown for 2019 is a general estimate constructed for the whole Central European domain (see Fig. 1) that is neither specific for individual countries nor for the year 2019. It assumes minimum emissions in July, whereas our observations show minimum emissions in August and September. Indeed, this shifted minimum of the seasonal cycle coincides with the summer holidays in Southwestern Germany, which are from August to mid-September.

We further investigate the consistency of the seasonal cycles from the bottom-up and the top-down estimates. For this, we explore the effect of using the monthly TNO bottom-up seasonal cycle for the a-priori emissions (see Fig. 4b). As expected, the phase of the a-posteriori seasonal cycle is in agreement with the TNO inventory in 2020. However, in 2019 the a-priori information pulls the summer emission minimum to July. With weakening regularization of the prior the inversion algorithm tries to shift the minimum of the a-posteriori seasonal cycle from July towards August and September. Due to the limited temporal degrees of freedom of the inversion this shifting results in artificially increasing the emissions in May 2019 and lowering them in October. Hence, these results might point to some inconsistencies in the seasonality of the TNO emissions in the main footprint of the Heidelberg observation site. In fact, correct phasing of the fossil emissions is essential when prescribed $ffCO_2$ emissions are used in CO_2 model inversions to separate the fossil from the biogenic contribution in atmospheric CO_2 observations and constrain CO_2 fluxes from the biosphere. Although these biospheric CO_2 signals are

typically estimated with observations from sites that are more remote and rural than the urban Heidelberg site, the correct seasonality in prescribed $ffCO_2$ emissions is still important when deducing the month-to-month variations in the biospheric CO_2 fluxes.

Overall, the (weekly averaged) ΔCO-based $\Delta ffCO_2$ record seems to be well suited to estimate (and validate) the seasonal cycle of bottom-up $ffCO_2$ emissions in the nearfield of the Heidelberg observation site. This is a very promising result, especially considering how simply the ΔCO-based $\Delta ffCO_2$ record was constructed. It is based on the two-year average $\Delta CO/\Delta ffCO_2$ ratio estimated from ^{14}C measurements on flask samples where a potential seasonal cycle in the $\Delta CO/\Delta ffCO_2$ ratios was fully neglected.

3.3 Robustness of the ΔCO-based $\Delta ffCO_2$ inversion results

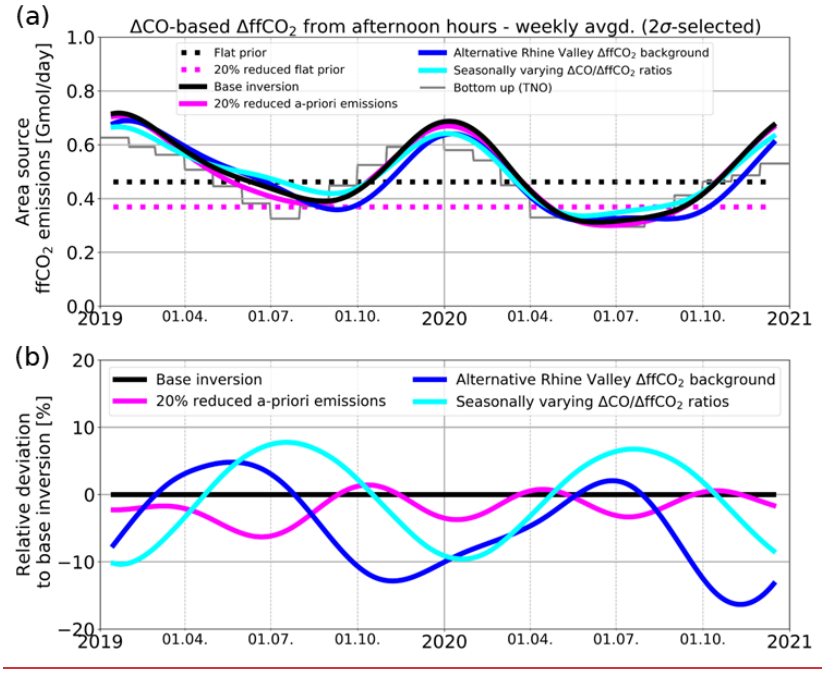

Figure 5: (a): Area source $ffCO_2$ emissions in the nearfield (blue surrounded area in Fig. 1b) of Heidelberg for different sensitivity runs. Shown are the a-posteriori results for 20% reduced flat a-priori emissions (solid magenta line), for an alternative Rhine Valley $\Delta ffCO_2$ background modelled with EDGAR emissions (blue) and for an assumed seasonal cycle in the $\Delta CO/\Delta ffCO_2$ ratios (cyan, see Fig. E1). As a reference, the a-posteriori result of the base inversion from Fig. 4a is shown in black. All a-posteriori results correspond to a 150% prior uncertainty. The dotted lines indicate the flat prior emissions (black) and the by 20% reduced prior emissions (magenta). (b): Relative deviations between the different a-posteriori area source emissions of the sensitivity runs and the base inversion in %.

In the following we investigate the robustness of the (weekly averaged) ΔCO-based $\Delta ffCO_2$ inversion results. For this, we (1) reduce the flat prior emissions by 20%, (2) assume a seasonal cycle in the $\Delta CO/\Delta ffCO_2$ ratios, and (3) apply an alternative Rhine Valley $\Delta ffCO_2$ background. We show in Fig. 5 the respective a-posteriori results for a prior uncertainty of 150%, which

constitutes enough weighting on the (weekly averaged) ΔCO-based ΔffCO_2 observations to reconstruct the seasonal cycle from the flat a-priori area source ffCO_2 emissions (see Fig. 4a). Moreover, the 150% prior uncertainty reduces the mean bias between the weekly averaged ΔCO-based ΔffCO_2 observations and the a-posteriori fits to 0.10±1.89 ppm (compared to the mean bias of 0.65±2.23 ppm, which one gets when using the flat prior emissions). Further increasing the prior uncertainty to 200% leads to only neglectable changes in the mean bias (0.11±1.88 ppm).

First, if the a-priori area source ffCO_2 emissions in the Rhine Valley domain are equally reduced by 20% (see dotted magenta line in Fig. 5a), the ΔCO-based ΔffCO_2 inversion manages to compensate for almost all of this bias (compare the magenta curves with the black curves in Fig. 5). The deviations between the a-posteriori emissions of the inversion runs with perturbed and unperturbed flat prior emissions is typically below 5% for all seasons (Fig. 5b). Accordingly, the a-posteriori seasonal cycle of the ffCO_2 emissions is hardly affected by a potential bias in the flat prior emissions. The deviations between the annual totals of the a-posteriori estimates of the perturbed and unperturbed prior inversion runs is only 2% for both years. This means that on an annual scale about 90% of this 20%-bias in the perturbed flat prior could be corrected for with the observational constraint.

With the second sensitivity test, we want to investigate the effect of the ΔCO/ΔffCO_2 ratios used to construct the ΔCO-based ΔffCO_2 record. For our base inversion, the ΔCO-based ΔffCO_2 record was constructed by using the average ΔCO/ΔffCO_2 ratio of 8.44±0.07 ppb/ppm, which was calculated from all flask samples collected in Heidelberg in 2019 and 2020. However, as discussed in Maier et al. (2023a), the ratio during summer with lower signals is hard to determine and thus less constrained. Indeed, the winter flasks show a slightly higher mean ΔCO/ΔffCO_2 ratio (8.52±0.08 ppb/ppm, R^2=0.89) compared to the summer flasks (8.08±0.17, R^2=0.36). The question is thus: How would our inversion results change if the ΔCO/ΔffCO_2 ratios would have a (small) seasonal cycle? For this, we assume a seasonal cycle in the ratios for the two years with 5% lower ratios in the summer half-year and correspondingly 5% larger ratios in the winter half-year, so that the two-year mean is still 8.44 ppb/ppm (see Fig. E1). Notice, that we use the ratios to calculate the Δff$CO_{2,MHD}$ excess compared to the MHD background site and then subtract the modelled Rhine Valley Δff$CO_{2,CE-RV}$ background to get the Δff$CO_{2,RV}$ observations for our Rhine Valley inversion (see Eq. 1). This effectively results in summer and winter ΔffCO_2 concentrations being more than 5% larger and lower, respectively, than the ΔffCO_2 concentrations based on the average ratio. Obviously, this leads to larger a-posteriori emissions (cyan curve in Fig. 5) during summer and lower emissions in winter compared to the base inversion results. The largest seasonal deviations to the base inversion a-posteriori emissions are 10%. Since by construction the mean of the seasonally varying ratios corresponds to the average ratio used for the base inversion, the effect on the annual totals of the a-posteriori ffCO_2 emissions is neglectable.

Finally, we investigate the impact of the lateral ΔffCO_2 boundaries on the area source ffCO_2 emissions estimates. For our base inversion, we used the high-resolution TNO emission inventory and WRF-STILT to model for the Heidelberg observation site

the $\Delta ffCO_2$ contributions from the European STILT domain outside the Rhine Valley (see Sect. 2.2.4). For the following sensitivity run (blue curve in Fig. 5), we model the Rhine Valley $\Delta ffCO_2$ background with $ffCO_2$ emissions based on the EDGAR emissions and with a coarser meteorology in STILT (see Sect. 2.2.4). The application of this alternative Rhine Valley $\Delta ffCO_2$ background leads to more than 10% lower emissions in the autumn of both years, which can be explained by strong deviations between the weekly averages of the two modelled background concentrations during these periods (see Fig. F1). Thus, the Rhine Valley background affects the seasonal cycle of the area source $ffCO_2$ emissions. During summer, the deviations to the base inversion results are below 5%. The annual totals of the area source $ffCO_2$ emissions around Heidelberg are 3% and 7% lower in the years 2019 and 2020, respectively, if the alternative Rhine Valley $\Delta ffCO_2$ background is used.

4 Discussion and Conclusions

In the present study we investigate the potential of ^{14}C-based and ΔCO-based $\Delta ffCO_2$ observations to evaluate the $ffCO_2$ emissions and their seasonal cycle in an urban region around the Heidelberg observation site. This urban area is characterized by complex topography and large spatial heterogeneity in $ffCO_2$ sources, including several nearby point sources. Thus, deficits in the transport model as well as inaccuracies in the driving meteorology and the prescribed point source emissions strongly impact the model-data mismatch at the observation site, which will be minimized by the inversion algorithm. We focus on the estimation of the $ffCO_2$ emissions from area sources, since the observations from the Heidelberg site with an air intake height of 30 m above the ground are not suitable to constrain the emissions of nearby point sources with elevated stack heights. Indeed, the analysis of the $\Delta CO/\Delta ffCO_2$ ratios in Maier et al. (2023a) showed that the Heidelberg observation site is hardly influenced by pure point source emission plumes. Moreover, we expect that point source emissions can be better quantified a-priori from bottom up compared to area source emissions. Therefore, we prescribe the better known point source $ffCO_2$ emissions in the inversion setup and only adjust the area source emissions in the Rhine Valley domain.

4.1 Can flask-based $\Delta ffCO_2$ observations be used to predict the seasonal cycle of $ffCO_2$ emissions at an urban site?

To investigate the potential of $\Delta ffCO_2$ observations to predict the seasonal cycle of the area source $ffCO_2$ emissions around Heidelberg, we applied temporally constant (flat) a-priori $ffCO_2$ emissions in our inversion system, such that all seasonal information comes from the atmospheric data. We have shown that ^{14}C-based $\Delta ffCO_2$ observations from almost 100 hourly flask samples collected in the two years 2019 and 2020 are not sufficient to reconstruct a robust seasonal cycle from the flat a-priori estimate. As the Bayesian inversion setup assumes a Gaussian distribution for the model-data mismatch, the inversion algorithm tries to primarily reduce the largest model-data differences. Therefore, we applied a 2σ selection to exclude the flask events with the largest model-data mismatches and thus worse model performances. However, the a-posteriori $ffCO_2$ emissions are still very sensitive to individual flask observations. This may suggest that the 2σ filter is not sufficient in a densely populated high fossil fuel environment like Heidelberg with a complex topography. Therefore, strong regularization through small a-

priori uncertainties (i.e. < 50% prior uncertainty, Fig. 3a) is needed in the case of flask observations to avoid large overfitting patterns in the inversion results.

Due to the fortunate circumstance of currently having similar heating and traffic emission ratios in the main footprint of Heidelberg, we decided to use the two-year average ^{14}C-based $\Delta CO/\Delta ffCO_2$ ratio from the flasks to construct a continuous ΔCO-based $\Delta ffCO_2$ record (see Maier et al., 2023a). By subsampling this ΔCO-based $\Delta ffCO_2$ record, we further investigate the potential of a uniform data coverage with one hypothetical afternoon flask per week to reliably estimate the seasonal cycle in the area source emissions. Indeed, several afternoon flask samples per week are needed, as well as an averaging of the flask observations within one week so that the overfitting of individual flask data is reduced. However, the situation should be better for real, e.g. sub-weekly, ^{14}C flasks compared to the subsampled ΔCO-based $\Delta ffCO_2$ record. As the applied two-year average $\Delta CO/\Delta ffCO_2$ ratio may be inappropriate for individual hours, this could amplify the sensitivity to the individual hypothetical flasks.

4.2 What is an appropriate averaging interval for urban observations?

The main advantage of the ΔCO-based $\Delta ffCO_2$ record is its continuous data coverage that allows an averaging so that the influence of individual hours with poor model performance on the inversion results is strongly reduced. The comparison of Fig. 3e with Fig. 3f and Fig. 4a clearly illustrates that the averaging of multiple hourly observations leads to a reduction of the a-posteriori flux variability. In this urban region, such an averaging is especially necessary because of the shortcomings in the STILT model and its driving meteorology to describe the transport and mixing of nearby point source emissions. Imagine that the plume of a point source arrives a few hours earlier or later at the observation site than simulated by STILT. In such cases, averaging is inevitable to prevent a wrong adjustment of the $ffCO_2$ emissions. Moreover, the STILT-VSI approach itself has its deficits as it assumes mean effective emission height profiles for all meteorological situations and ignores the stack heights of individual power plants. Furthermore, the VSI approach still relies on a correct vertical mixing in STILT and an accurate point source emission inventory. Whereas in Maier et al. (2022) we could show that the VSI approach strongly improves the agreement between modelled and observed $\Delta ffCO_2$ concentrations from two-week integrated samples, it thus still may overestimate the point source contributions for individual hours. Therefore, an averaging of the observations is very helpful when a transport model like STILT is used to describe the transport and mixing of nearby point source emissions.

We investigate how to appropriately average the observational and modelled data. Ideally, the a-posteriori area source $ffCO_2$ emissions are independent of an incorrect modelling of the point source emissions. Thus, they should not be affected by whether the a-priori point source emissions are fixed or adjustable in the inversion framework, provided that the point source emissions are well represented in the emission inventory. We found that an averaging interval of one week limits the differences between the a-posteriori area source $ffCO_2$ emissions of the inversion runs with fixed and adjustable point source emissions to below 30% for all seasons. This deviation can be used as a measure for the uncertainty of the a-posteriori area

source $ffCO_2$ emissions that is induced by an inadequate modelling of the point source emissions. A longer, e.g. monthly, averaging interval further reduces this difference (see Appendix C), but comes along with an averaging over very different meteorological situations and thus reduces the spatiotemporal information comprised in the observations. This might be especially important if there are several observation sites, and the inversion system optimizes the $\Delta ffCO_2$ gradients between these different stations. The averaging interval of a week corresponds to the typical length scale of synoptic weather patterns. Therefore, the model-data-mismatch error has anyhow been increased to account for the potential correlations between the hourly observations within one week. The weekly averaging should, thus, not destroy too much information. An averaging interval of one week should thus be seen as a compromise between reducing the impact of hours with an inadequate model performance and using as much observational information as possible.

4.3 What is the potential of ΔCO-based $\Delta ffCO_2$ to estimate the seasonal cycle in urban $ffCO_2$ emissions?

The weekly averaged ΔCO-based $\Delta ffCO_2$ observations lead to robust seasonal cycles in $ffCO_2$ emissions with a plausible amplitude and phasing, based on comparison with the TNO inventory. Figure G1 further compares the TNO $ffCO_2$ emissions in the nearfield area of Heidelberg (blue outlined area in Fig. 1b) with emissions from the EDGAR inventory (as introduced in Sect. 2.2.4) and the GridFEDv2021.2 inventory (Jones et al., 2021). While the EDGAR emissions are on average about 25% lower than the TNO emissions over the two years 2019 and 2020, the GridFED inventory shows ca. 23% larger emissions than TNO. This illustrates the uncertainty of the emission inventories on the regional scales. In 2019, the amplitude and phasing of the seasonal cycle are very similar for the EDGAR and TNO inventory. However, in spring 2020 the normalized seasonal cycles of the two inventories show differences of up to roughly 20%, which can be explained by the fact that the shown seasonal cycle of the EDGAR inventory does not take into account the COVID-19 restrictions. In contrast, the seasonal cycles from GridFED include the effect of the COVID-19 restrictions in spring 2020 similar to TNO but show a smaller seasonal cycle amplitude compared to EDGAR and TNO in 2019. Overall, the seasonal cycles of our top-down estimate are in the range covered by all three bottom-up inventories, thus inferring that we could indeed reliably reconstruct the amplitude and the phasing of the seasonal cycle from flat a-priori area source $ffCO_2$ emissions with the ΔCO-based $\Delta ffCO_2$ observations.

We further could detect the COVID-19 signal in 2020, which is characterized by lower emissions compared to 2019 and a very steep decline in the emissions in spring 2020 (cf. Fig. D1). This is in accordance with what is reported by TNO for 2020. However, for 2019 our ΔCO-based $\Delta ffCO_2$ results suggest the summer minimum of the (restricted) Rhine Valley area source $ffCO_2$ emissions to be in August and September (instead of July), when local summer holidays take place in that part of Germany. This result of the Heidelberg inversion might thus point to some inconsistencies in the seasonality of TNO emissions in the footprint of the station. The correct phasing of the fossil emissions is essential when prescribed $ffCO_2$ emissions and associated forward modelling results are used in atmospheric transport inversions to constrain the CO_2 fluxes from the biosphere.

In contrast to the inversion with flask-^{14}C-based $\Delta ffCO_2$ observations, the ΔCO-based $\Delta ffCO_2$ inversion with weekly averaging allows a weakening of the regularization strength without generating unrealistic variabilities in the seasonal cycle of the $ffCO_2$ emissions. This implies that the a-posteriori results are less dependent on a potential bias in the a-priori emissions (cf. Fig. G1). Indeed, a sensitivity run with a 20% reduced flat prior estimate for the area source $ffCO_2$ emissions leads to similar results as the base inversion run with unperturbed prior estimate, when sufficiently large prior uncertainties are used. Thus, the ΔCO-based $\Delta ffCO_2$ inversion is able to simultaneously reconstruct the seasonal cycle from a flat prior and correct a potential bias in the total a-priori emissions.

However, the ΔCO-based $\Delta ffCO_2$ inversion results strongly depend on a potential bias in the $\Delta CO/\Delta ffCO_2$ ratios that are applied to calculate the $\Delta ffCO_2$ estimates. Since there is no evidence for a strong seasonal cycle in the $\Delta CO/\Delta ffCO_2$ ratios at the Heidelberg observation site, we used a constant average $\Delta CO/\Delta ffCO_2$ ratio to calculate the ΔCO-based $\Delta ffCO_2$ record for the two years 2019 and 2020 (see Maier et al., 2023a). But due to the low signals and the weak correlation between ΔCO and $\Delta ffCO_2$ during summer, it is hard to determine separate summer ratios. Nevertheless, our results indicate that there might be a small seasonal cycle on the order of 5% in the ratio. We have shown that a hypothetical seasonal cycle with 5% lower and 5% larger ratios in summer and winter, respectively, would lead to changes in the area source $ffCO_2$ emissions of up to 10% for individual seasons. This emphasizes the importance of a thorough determination of the $\Delta CO/\Delta ffCO_2$ ratios to prevent biases in estimates of total fluxes *and* the seasonal cycle of the $ffCO_2$ emissions.

Indeed, we are currently in a fortunate situation in Heidelberg, since the emission ratios of the traffic and heating sectors seem to be quite similar in the main footprint of the station (see Maier et al., 2023a). Hence, despite the varying share of traffic and heating over the course of a year, this allowed the usage of a constant average flask-based $\Delta CO/\Delta ffCO_2$ ratio for constructing the ΔCO-based $\Delta ffCO_2$ record. Of course, it is much more challenging to determine continuous ΔCO-based $\Delta ffCO_2$ estimates for stations where the $\Delta CO/\Delta ffCO_2$ ratios show large seasonal or even diurnal variability. In principle, also bottom-up estimates of the seasonal contributions of each $ffCO_2$ sector and its characteristic $CO/ffCO_2$ emission ratio could be used to construct the seasonal cycle of the $\Delta CO/\Delta ffCO_2$ ratios. However, in the companion paper (Maier et al., 2023a) we show that there can be large discrepancies between ^{14}C-based and inventory-based $\Delta CO/\Delta ffCO_2$ ratios. Therefore, we recommend to validate those bottom-up ratios by observations before using them to estimate a continuous $\Delta ffCO_2$ record.

The ΔCO-based $\Delta ffCO_2$ inversion can be seen as a simplification of a multi-species inversion, which is based on collocated CO_2 and CO observations. Such a multi-species inversion exploits the fact that the collocated CO_2 and CO observations are affected by the same atmospheric transport and that these two species have partially overlapping emission patterns (Boschetti et al., 2018). Boschetti et al. (2018) show that the consideration of these inter-species correlations leads to a reduction in the respective a-posteriori uncertainties of the $ffCO_2$ (and CO) emissions. While our ΔCO-based $\Delta ffCO_2$ inversion assumes a constant but observation-based $\Delta CO/\Delta ffCO_2$ ratio, the multi-species inversion intrinsically considers the spatiotemporal

variability of the ratios. However, this requires reliable a-priori estimates of the CO/ffCO$_2$ emission ratios and their uncertainties, as well as neglectable non-fossil CO sources and sinks.

A common challenge in regional inversions is the determination of the lateral boundary conditions (Munassar et al., 2023). In this study, we used two different emission inventories and meteorological fields to estimate the ΔffCO$_2$ background for the Rhine Valley domain by modelling the contributions from the Central European ffCO$_2$ emissions outside the Rhine Valley. For individual seasons the a-posteriori area source ffCO$_2$ emissions around Heidelberg can differ by more than 10%. This highlights the strong need for appropriate boundary conditions. In Europe, the Integrated Carbon Observation System (ICOS, Heiskanen et al., 2022) provides high-quality atmospheric in-situ data from a network of tall-tower stations that cover a large part of the European continent. These observations may help to verify the ffCO$_2$ emissions in Europe. Then, the optimized European ffCO$_2$ emissions could be used to estimate more reliably the ΔffCO$_2$ background for the Rhine Valley domain.

Overall, our results demonstrate that the weekly averaged ΔCO-based ΔffCO$_2$ observations are currently well suited to investigate the amplitude and the phasing of the seasonal cycle of the area source ffCO$_2$ emissions in the main footprint of the Heidelberg observation site. The different sensitivity runs suggest that ΔCO-based ΔffCO$_2$ allows a reconstruction of this seasonal cycle from temporally constant a-priori estimates with an uncertainty of below ca. 30% for all seasons. Thus, we recommend applying this ΔCO-based ΔffCO$_2$ inversion at further urban sites with a strong heterogeneity in the local ffCO$_2$ sources if the ΔCO/ΔffCO$_2$ ratios can be determined accurately. If ratios from bottom-up inventories are not trusted or the urban region is influenced by CO emissions from the biosphere, the ratios are most reliably calculated from ^{14}C flasks. Then, at least some of the summer ^{14}C flasks should be collected during situations with significant CO and ffCO$_2$ signals, so that a possible seasonal cycle in the ΔCO/ΔffCO$_2$ ratios could be identified. At remote sites, such as at several ICOS atmosphere stations with low ffCO$_2$ signals and predominant biosphere influence, the calculation of ΔCO/ΔffCO$_2$ ratios and the construction of a bias-free ΔCO-based ΔffCO$_2$ record might be more challenging than at an urban site. However, the model performance is expected to be better at remote sites with a typically higher air intake above the ground and a much lower heterogeneity in the surrounding ffCO$_2$ sources with minor influences from nearby point sources. Consequently, the outcome of our urban study cannot directly be transferred to remote sites; further studies are needed to investigate the potential of ^{14}C-based versus ΔCO-based ΔffCO$_2$ to estimate ffCO$_2$ emissions at such sites.

Finally, the good performance of the continuous but less precise ΔCO-based ΔffCO$_2$ observations in our regional inversion suggests that there may be potential for continuously measured ^{14}CO$_2$ (e.g. via optical spectrometry) to estimate urban ffCO$_2$ emissions, even if those continuous ^{14}CO$_2$ measurements have larger uncertainties.

Appendix A: Description of the CarboScope inversion framework

A detailed description of the CarboScope inversion system can be found in Rödenbeck (2005). In the following we summarize the main characteristics for reference.

In this study, the CarboScope inversion framework is used to minimize the model-data mismatch $\boldsymbol{m}$ between observed and modelled $\Delta ffCO_2$ concentrations. For this, the $ffCO_2$ flux field $\boldsymbol{f}$ is written in terms of a fixed a-priori estimate $\boldsymbol{f}_{\mathrm{fix}}$ and a vector $\boldsymbol{p}$ with dimensionless adjustable parameters

$$\boldsymbol{f} = \boldsymbol{f}_{\mathrm{fix}} + \boldsymbol{F}\boldsymbol{p} \qquad \text{(A.4.1)}$$

where the matrix **F** describes the uncertainty of the a-priori fluxes and their spatiotemporal correlations. The a-priori realization of the parameters $\boldsymbol{p}_{\mathrm{pri}}$ is assumed to have a zero mean, i.e. $\langle \boldsymbol{p}_{\mathrm{pri}} \rangle = 0$, and the variance $\langle \boldsymbol{p}_{\mathrm{pri}} \boldsymbol{p}_{\mathrm{pri}}^{\mathrm{T}} \rangle = \frac{1}{\mu}\mathbf{1}$, where $\mathbf{1}$ is the identity matrix and μ a scaling factor. This leads to the following cost function:

$$J = \frac{1}{2}\boldsymbol{m}^{\mathrm{T}}\boldsymbol{Q}_{\boldsymbol{m}}^{-1}\boldsymbol{m} + \frac{\mu}{2}\boldsymbol{p}^{\mathrm{T}}\boldsymbol{p} + C \qquad \text{(A.4.2)}$$

The first term of this cost function describes the data constraint, which is weighted by the model-data mismatch covariance matrix $\boldsymbol{Q}_{\boldsymbol{m}}$. The a-priori constraint is included in the second term of the cost function. It is scaled by the parameter μ, which effectively represents the ratio between a-priori and data constraint (e.g., the a-priori term vanishes for $\mu \rightarrow 0$, in accordance with the a-priori covariance matrix $\boldsymbol{Q}_{f,\mathrm{pri}} = \frac{1}{\mu}\boldsymbol{F}\boldsymbol{F}^{\mathrm{T}}$ going to infinity. Note that $\boldsymbol{Q}_{f,\mathrm{pri}}$ does not explicitly appear in the CarboScope implementation). The last constant C contains all terms that are independent of $\boldsymbol{p}$.

The minimum of the cost function is calculated from

$$\left.\frac{\partial J}{\partial \boldsymbol{p}^{\mathrm{T}}}\right|_{\boldsymbol{p}=\langle \boldsymbol{p}_{\mathrm{post}} \rangle} = 0 \qquad \text{(A.4.3)}$$

where $\boldsymbol{p}_{\mathrm{post}}$ describes the a-posteriori realizations of the parameter vector $\boldsymbol{p}$. For this, a conjugate gradient algorithm is used, which is described in detail in Rödenbeck (2005).

Appendix B: Fits to the flask observations

In Fig. B1 we show the agreement between the flat prior and the different a-posteriori-based model results and the flask observations. It illustrates that the inversion mainly reduces the largest model-data mismatches of individual winter flasks and the negative model-data mismatches in summer 2020.

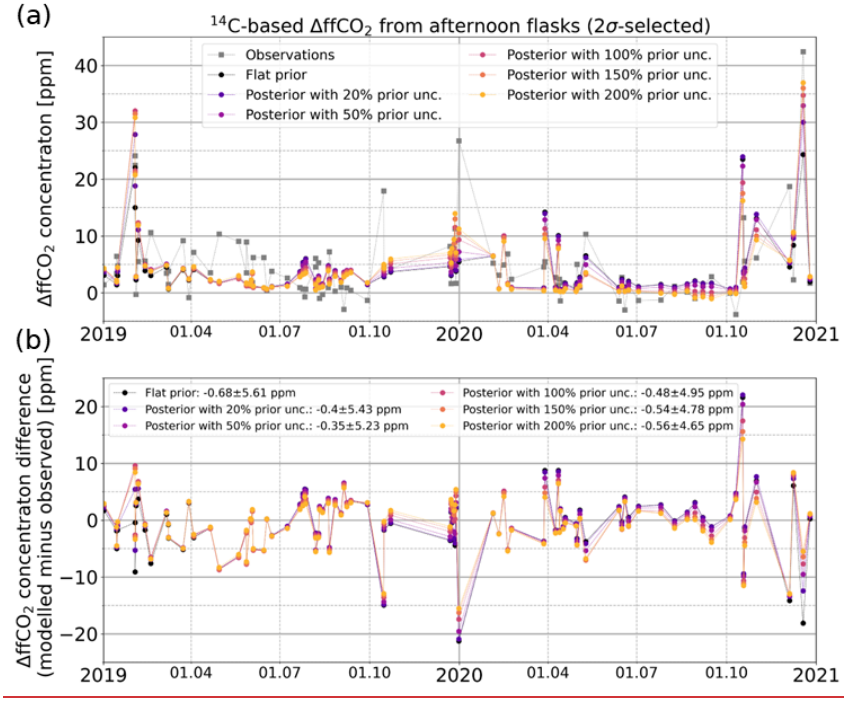

Figure B1: Comparison between the observed ^{14}C-based ΔffCO$_2$ concentrations from the flasks and the modelled ΔffCO$_2$ concentrations based on the flat prior (black) and the different a-posteriori emissions with prior uncertainties between 20% and 200% (coloured).

Appendix C: Impact of the averaging interval and additional degrees of freedom for the point sources emissions

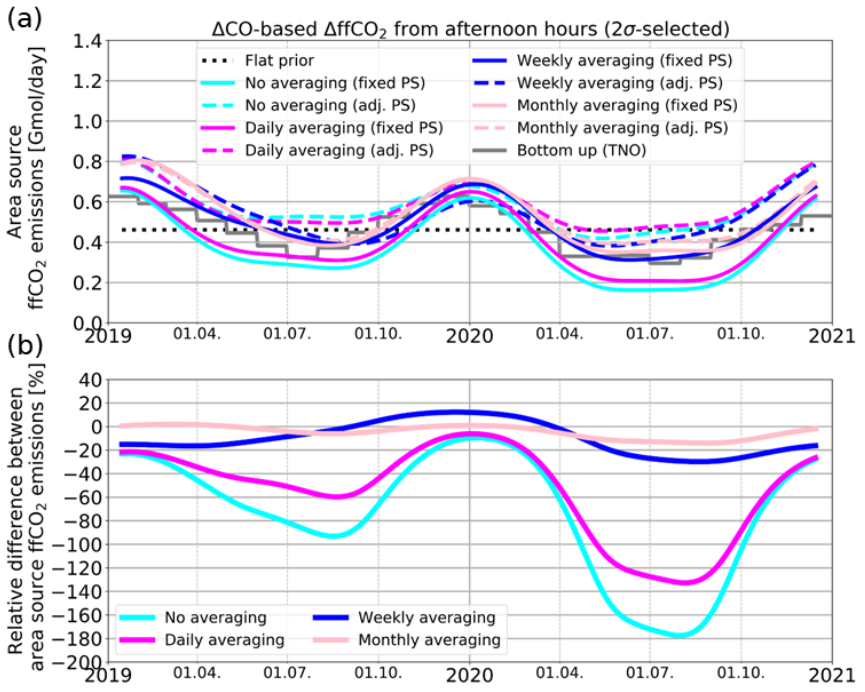

Figure C1: (a): Area source $ffCO_2$ emissions in the nearfield (blue outlined area in Fig. 1b) of Heidelberg. Shown are the results of the ΔCO-based $\Delta ffCO_2$ inversion with fixed point sources (solid lines, "fixed PS") and adjustable point sources (dashed lines, "adj. PS") for different averaging intervals ranging from no averaging at all (cyan) to daily averaging of the five hours (11 – 16 UTC) of each afternoon (magenta) and weekly (blue) and monthly (pink) averaging. All a-posteriori results correspond to a 150% prior uncertainty. The flat a-priori emissions and the bottom-up emissions are shown as a reference in black and grey, respectively. (b): Relative differences (fixed PS minus adj. PS) between the a-posteriori area source $ffCO_2$ emissions of the inversion runs with adjustable and fixed point source emissions in %.

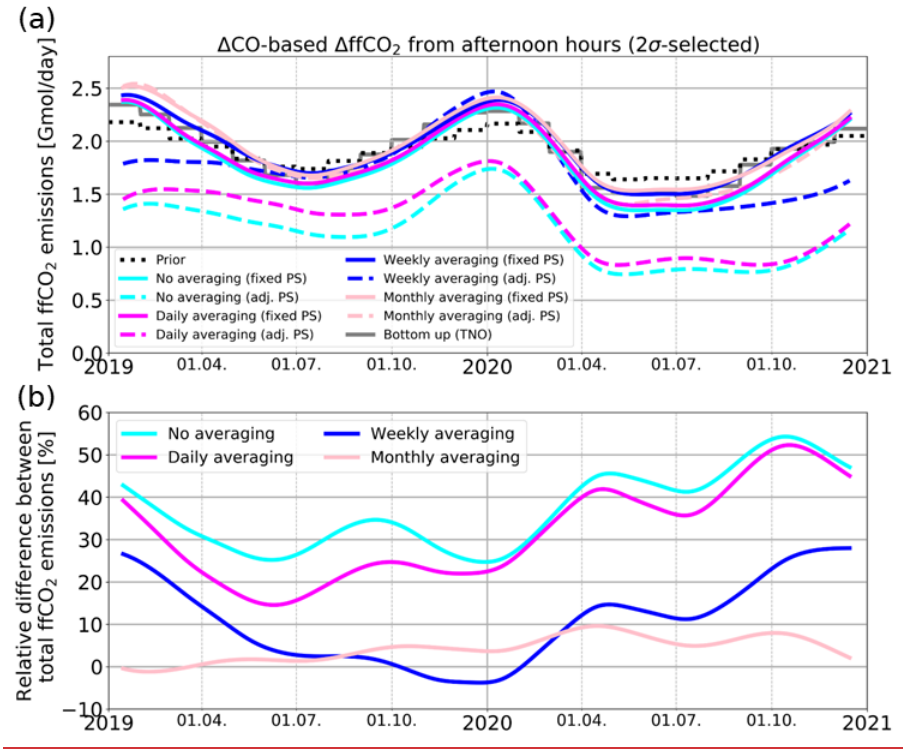

Figure C2: (a): Area plus point source (i.e. "total") $ffCO_2$ emissions in the nearfield (blue outlined area in Fig. 1b) of Heidelberg. Shown are the results of the ΔCO-based $\Delta ffCO_2$ inversion with fixed point sources (solid lines, "fixed PS") and adjustable point sources (dashed lines, "adj. PS") for different averaging intervals ranging from no averaging at all (cyan) to daily averaging of the five hours (11 – 16 UTC) of each afternoon (magenta) and weekly (blue) and monthly (pink) averaging. All a-posteriori results correspond to a 150% prior uncertainty. The a-priori emissions and the bottom-up emissions are shown as a reference in black and grey, respectively. (b): Relative differences (fixed PS minus adj. PS) between the a-posteriori area source $ffCO_2$ emissions of the inversion runs with adjustable and fixed point source emissions in %.

To investigate the influence of inadequate point source modelling on the a-posteriori area source $ffCO_2$ emissions, we use two different ΔCO-based $\Delta ffCO_2$ inversion setups: (1) an inversion with fixed point source emissions ("INV_fix") and (2) an inversion with adjustable point source emissions ("INV_adj"). The first inversion setup corresponds to the inversion described in Sect. 2. It optimizes the flat a-priori area source emissions by using fixed monthly point source emissions. The second inversion setup optimizes both, the flat a-priori area source emissions, and the monthly a-priori point source emissions. Thereby, the point source emissions from the energy production and the industry sector, respectively, get the same temporal (i.e. "Filt3T" in CarboScope notation, see Sect. 2.2.6) and spatial (i.e. one spatial scaling factor) degrees of freedom like the area source emissions. Ideally, both inversion setups should lead to the same a-posteriori area source emissions, meaning that the modelling of the better known point source emissions has no influence on the area source emission estimates. Obviously, this is not the case. If the observed and modelled hourly $\Delta ffCO_2$ concentrations (i.e. the model-data mismatches) are not averaged over a certain period of time, the INV_fix inversion leads to much lower area source emissions estimates than the INV_adj inversion (see cyan curves in Fig. C1). For individual seasons, e.g. in summer 2020, the differences are larger than

150%. Thus, the INV_fix inversion tends to decrease the area source emissions to compensate for an inadequate modelling of the (fixed) point source emissions. This indicates that the transport model (even with the VSI approach) and/or the TNO emission inventory seems to overestimate the contributions from point sources at the Heidelberg observation site for individual hours.

The averaging over one afternoon (magenta curve in Fig. C1) leads only to minor improvements; there are still deviations larger than 100% in summer 2020. In contrast, the averaging interval of one week (blue curve) limits the largest deviations in summer 2020 to below 30%. Averaged over the two years 2019 and 2020, these deviations between the INV_fix and INV_adj a-posteriori area source emissions are less than 10%. A monthly averaging interval (pink curve) further reduces the deviations to below 20% in summer 2020.

We also investigate if the sum of the a-posteriori area source and point source emissions is similar for the INV_fix and the INV_adj inversion runs (see Fig. C2). If no averaging or only a daily averaging is applied, the INV_adj run leads to up to 50% lower total (i.e. area plus point source) $ffCO_2$ emissions than the INV_fix run. This again shows that the point source emissions are strongly reduced in the INV_adj inversion run. A weekly averaging (blue curve) restricts the relative differences between INV_fix and INV_adj to below ca. 20% if the first and the last two months of the two-year period are disregarded. The monthly averaging shows again the smallest differences (below 10%) between the INV_fix and the INV_adj run.

Fig. C3 shows the comparison between the modelled $\Delta ffCO_2$ concentrations based on the INV_fix and INV_adj a-posteriori emissions and the ΔCO-based $\Delta ffCO_2$ observations if a weekly averaging is applied (i.e. all hourly entries within one week are averaged in the model-data mismatch vector). The mean bias and the standard deviation between weekly averaged observed and modelled $\Delta ffCO_2$ is very similar for both inversion runs (0.10±1.89 ppm in the case of INV_fix and 0.13±1.80 ppm in the case of INV_adj). For comparison, the flat prior emissions lead to a mean bias of 0.65±2.23 ppm. Hence, there are no significant changes in the fits to the observational data when additional degrees of freedom are introduced for the point source emissions.

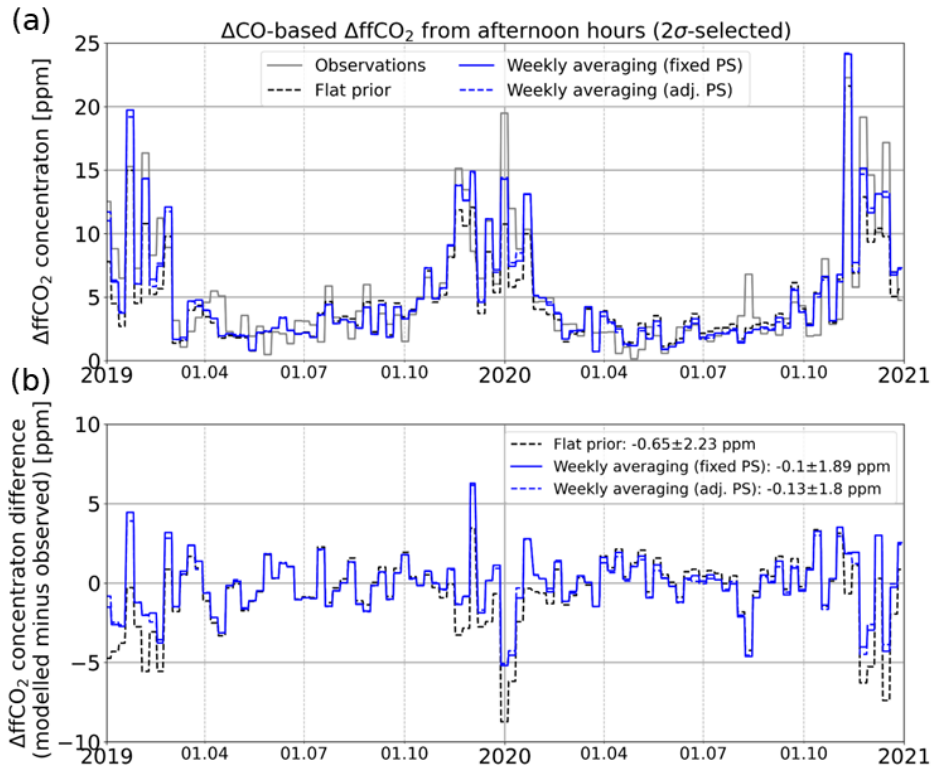

Figure C3: Comparison between the weekly averaged observed ΔCO-based $\Delta ffCO_2$ concentrations (grey) and the modelled $\Delta ffCO_2$ concentrations based on the flat prior (black) and the a-posteriori emissions with a prior uncertainty of 150% (blue). Shown are the results for the standard INV_fix inversion setup with fixed point source emissions (solid) and the INV_adj inversion setup with adjustable point source emissions (dashed). In both inversion setups the hourly entries of the model-data mismatch vector within one week were averaged.

Appendix D: Anomaly in the seasonal cycle of the area source $ffCO_2$ emissions in 2020

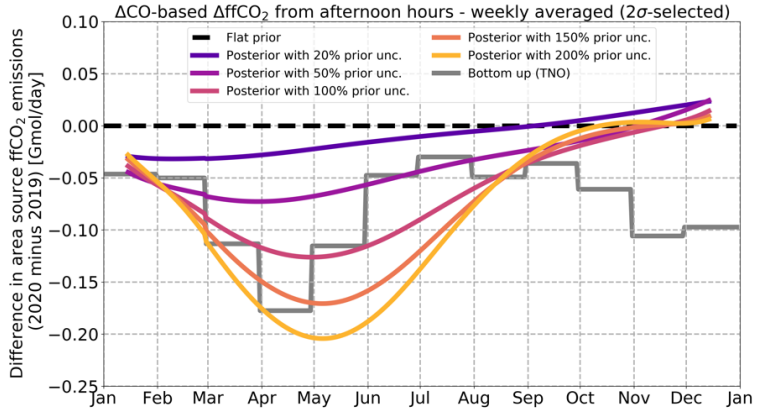

Figure D1: Difference in the nearfield area source $ffCO_2$ emissions (in the blue outlined area in Fig. 1) between 2020 and 2019. Shown are the results of the ΔCO-based $\Delta ffCO_2$ inversion with fixed point sources and temporally flat prior emissions (cf. Fig. 4a).

Appendix E: Hypothetical seasonal cycle in the ΔCO/ΔffCO₂ ratios

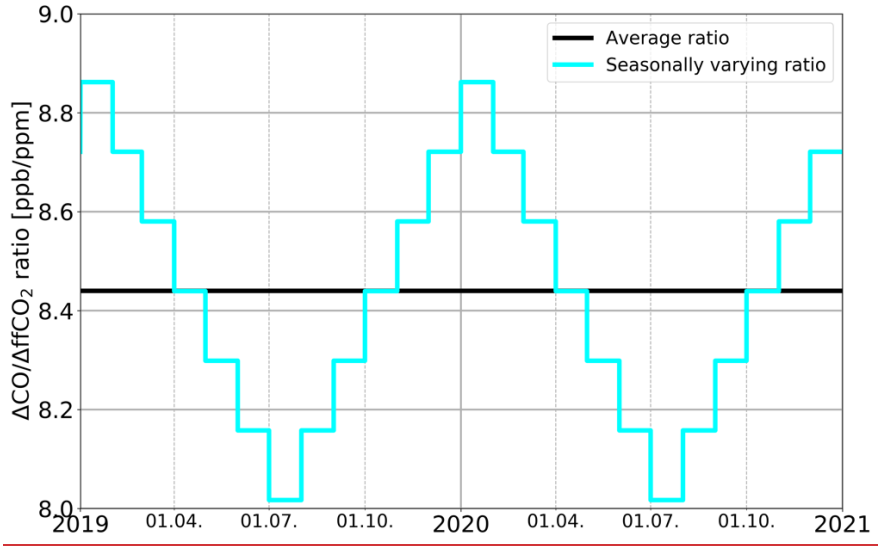

Figure E1: Average ΔCO/ΔffCO₂ ratio (black) and hypothetical seasonal varying ratio (cyan) used to construct the ΔCO-based ΔffCO₂ record for the base inversion (Fig. 4) and the sensitivity inversion run (cyan curve in Fig. 5), respectively.

Appendix F: Comparison between two modelled Rhine Valley ΔffCO₂ backgrounds

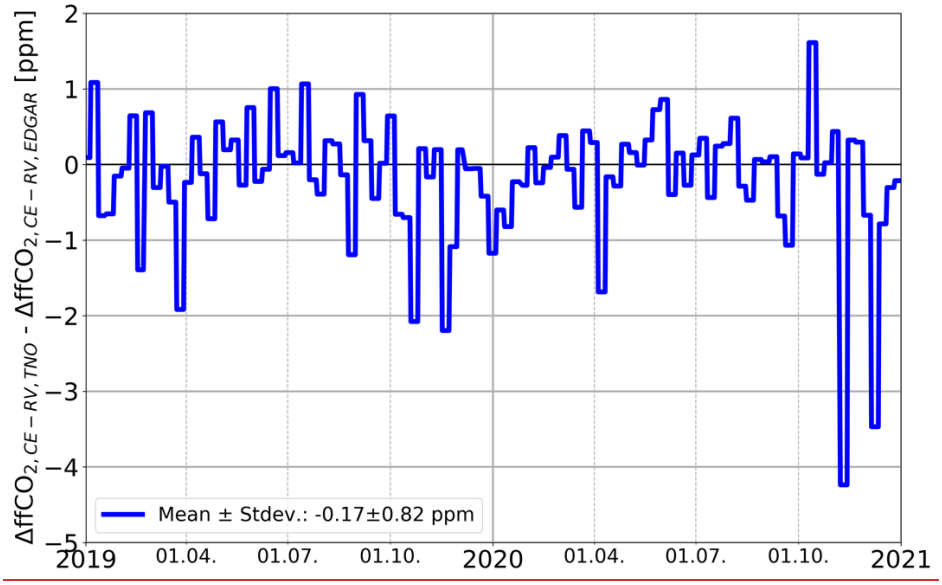

Figure F1: Difference between the Rhine Valley background modelled with TNO emissions ($\Delta ffCO_{2,CE\text{-}RV,TNO}$) and the Rhine Valley background modelled with EDGAR emissions ($\Delta ffCO_{2,CE\text{-}RV,EDGAR}$). Shown are weekly averages for afternoon situations.

Appendix G: Comparison between TNO and other emission inventories

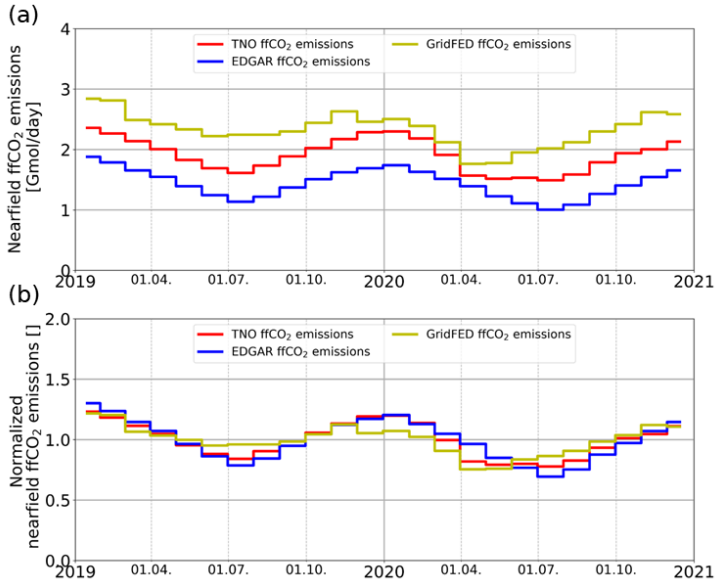

Figure G1: (a) Comparison between the TNO (red), EDGAR (blue) and GridFED (yellow) $ffCO_2$ emissions within the nearfield area of Heidelberg (blue outlined area in Fig. 1b). (b) shows the respective normalized nearfield $ffCO_2$ emissions.

Data availability

We used the ^{14}C- and ΔCO-based $\Delta ffCO_2$ data published with Maier et al. (2023a). They can be found in Maier et al. (2023c).

Author contribution

FM designed the study together with all co-authors. FM performed the inverse modelling and processed the inversion results. CR helped with applying the CarboScope inversion framework for the Rhine Valley domain. CG modelled the alternative Rhine Valley $\Delta ffCO_2$ background with emissions based on EDGAR. The various inversion results were discussed by all authors. FM wrote the manuscript with help of all co-authors.

Competing interests

Some authors are members of the editorial board of ACP. The peer-review process was guided by an independent editor, and the authors have also no other competing interests to declare.

Acknowledgement

We are grateful to the staff of TNO at the Department of Climate, Air and Sustainability in Utrecht for providing the emission inventory as well as to Julia Marshall and Michał Gałkowski for computing and processing the high-resolution WRF meteorology in the Rhine Valley.

Financial support

This research has been supported by the German Weather Service (DWD), the ICOS Research Infrastructure and VERIFY (grant no. 776810, Horizon 2020 Framework). The ICOS Central Radiocarbon Laboratory is funded by the German Federal Ministry of Transport and Digital Infrastructure.

References

Andres, R. J., Boden, T. A., Bréon, F.-M., Ciais, P., Davis, S., Erickson, D., Gregg, J. S., Jacobson, A., Marland, G., Miller, J., Oda, T., Olivier, J. G. J., Raupach, M. R., Rayner, P., and Treanton, K.: A synthesis of carbon dioxide emissions from fossil-fuel combustion, Biogeosciences, 9, 1845–1871, https://doi.org/10.5194/bg-9-1845-2012, 2012.

Basu, S., Miller, J. B., and Lehman, S.: Separation of biospheric and fossil fuel fluxes of CO2 by atmospheric inversion of CO2 and 14CO2 measurements: Observation System Simulations, Atmos. Chem. Phys., 16, 5665–5683, https://doi.org/10.5194/acp-16-5665-2016, 2016.

Basu, S., Lehman, S. J., Miller, J. B., Andrews, A. E., Sweeney, C., Gurney, K. R., Xue, X., Southon, J., and Tans, P. P.: Estimating US fossil fuel CO_2 emissions from measurements of ^{14}C in atmospheric CO_2, PNAS 117(24): 13300–13307, https://doi.org/10.1073/pnas.1919032117, 2020.

Bergamaschi, P., Danila, A., Weiss, R. F., Ciais, P., Thompson, R. L., Brunner, D., Levin, I., Meijer, Y., Chevallier, F., Janssens-Maenhout, G., Bovensmann, H., Crisp, D., Basu, S., Dlugokencky, E., Engelen, R., Gerbig, C., Günther, D., Hammer, S., Henne, S., Houweling, S., Karstens, U., Kort, E., Maione, M., Manning, A. J., Miller, J., Montzka, S., Pandey, S., Peters, W., Peylin, P., Pinty, B., Ramonet, M., Reimann, S., Röckmann, T., Schmidt, M., Strogies, M., Sussams, J., Tarasova, O., van Aardenne, J., Vermeulen, A. T., and Vogel, F.: Atmospheric monitoring and inverse modelling for verification of greenhouse gas inventories, EUR 29276 EN, Publications Office of the European Union, Luxembourg, ISBN 978-92-79-88938-7, JRC111789, https://doi.org/doi:10.2760/759928, 2018.

Boschetti, F., Thouret, V., Maenhout, G. J., Totsche, K. U., Marshall, J., and Gerbig, C.: Multi-species inversion and IAGOS airborne data for a better constraint of continental-scale fluxes, Atmos. Chem. Phys., 18, 9225–9241, https://doi.org/10.5194/acp-18-9225-2018, 2018.

Ciais, P., D. Crisp, H. Denier Van Der Gon, R. Engelen, M. Heimann, G. Janssens-Maenhout, P. Rayner, and M. Scholze: Towards a European Operational Observing System to Monitor Fossil CO_2 Emissions. Final Report from the Expert Group, European Commission, October 2015, ISBN 978-92-79- 53482-9, doi:10.2788/350433, 2015. Available at https://www.copernicus.eu/sites/default/files/2019-09/CO2_Blue_report_2015.pdf, Last access: December 01, 2022.

Dellaert, S., Super, I., Visschedijk, A., and Denier van der Gon, H.: High resolution scenarios of CO_2 and CO emissions, CHE deliverable D4.2, 2019. Available at https://www.che-project.eu/sites/default/files/2019-05/CHE-D4-2-V1-0.pdf, Last access: March 28, 2023.

Denier van der Gon, H., Kuenen, J., Boleti, E., Maenhout, G., Crippa, M., Guizzardi, D., Marshall, J., and Haussaire, J.: Emissions and natural fluxes Dataset, CHE deliverable D2.3, 2019. Available at https://www.che-project.eu/sites/default/files/2019-02/CHE-D2-3-V1-1.pdf, Last access: March 28, 2023.

Duren, R., and Miller, C.: Measuring the carbon emissions of megacities, Nature Clim Change 2, 560–562, https://doi.org/10.1038/nclimate1629, 2012.

Friedlingstein, P., O'Sullivan, M., Jones, M. W., Andrew, R. M., Gregor, L., Hauck, J., Le Quéré, C., Luijkx, I. T., Olsen, A., Peters, G. P., Peters, W., Pongratz, J., Schwingshackl, C., Sitch, S., Canadell, J. G., Ciais, P., Jackson, R. B., Alin, S. R., Alkama, R., Arneth, A., Arora, V. K., Bates, N. R., Becker, M., Bellouin, N., Bittig, H. C., Bopp, L., Chevallier, F., Chini, L. P., Cronin, M., Evans, W., Falk, S., Feely, R. A., Gasser, T., Gehlen, M., Gkritzalis, T., Gloege, L., Grassi, G., Gruber, N., Gürses, Ö., Harris, I., Hefner, M., Houghton, R. A., Hurtt, G. C., Iida, Y., Ilyina, T., Jain, A. K., Jersild, A., Kadono, K., Kato, E., Kennedy, D., Klein Goldewijk, K., Knauer, J., Korsbakken, J. I., Landschützer, P., Lefèvre, N., Lindsay, K., Liu, J., Liu, Z., Marland, G., Mayot, N., McGrath, M. J., Metzl, N., Monacci, N. M., Munro, D. R., Nakaoka, S.-I., Niwa, Y., O'Brien, K., Ono, T., Palmer, P. I., Pan, N., Pierrot, D., Pocock, K., Poulter, B., Resplandy, L., Robertson, E., Rödenbeck, C., Rodriguez, C., Rosan, T. M., Schwinger, J., Séférian, R., Shutler, J. D., Skjelvan, I., Steinhoff, T., Sun, Q., Sutton, A. J., Sweeney, C., Takao, S., Tanhua, T., Tans, P. P., Tian, X., Tian, H., Tilbrook, B., Tsujino, H., Tubiello, F., van der Werf, G. R., Walker, A. P., Wanninkhof, R., Whitehead, C., Willstrand Wranne, A., Wright, R., Yuan, W., Yue, C., Yue, X., Zaehle, S., Zeng, J., and Zheng, B.: Global Carbon Budget 2022, Earth Syst. Sci. Data, 14, 4811–4900, https://doi.org/10.5194/essd-14-4811-2022, 2022.

Gamnitzer, U., Karstens, U., Kromer, B., Neubert, R. E. M., Meijer, H. A. J., Schroeder, H., and Levin, I.: Carbon monoxide: A quantitative tracer for fossil fuel CO_2?, J. Geophys. Res., 111, D22302, https://doi.org/10.1029/2005JD006966, 2006.

Graven, H., Fischer, M. L., Lueker, T., Jeong, S., Guilderson, T. P., Keeling, R. F., Bambha, R., Brophy, K., Callahan, W., Cui, X., Frankenberg, C., Gurney, K. R., LaFranchi, B. W., Lehman, S. J., Michelsen, H., Miller, J. B., Newman, S., Paplawsky, W., Parazoo, N. C., Sloop, C., and Walker, S. J.: Assessing fossil fuel CO_2 emissions in California using atmospheric observations and models, Environ. Res. Lett., 13, 065007, https://dx.doi.org/10.1088/1748-9326/aabd43, 2018.

Heiskanen, J., Brümmer, C., Buchmann, N., Calfapietra, C., Chen, H., Gielen, B., Gkritzalis, T., Hammer, S., Hartman, S., Herbst, M., Janssens, I. A., Jordan, A., Juurola, E., Karstens, U., Kasurinen, V., Kruijt, B., Lankreijer, H., Levin, I., Linderson, M., Loustau, D., Merbold, L., Myhre, C. L., Papale, D., Pavelka, M., Pilegaard, K., Ramonet, M., Rebmann, C., Rinne, J., Rivier, L., Saltikoff, E., Sanders, R., Steinbacher, M., Steinhoff, T., Watson, A., Vermeulen, A. T., Vesala, T., Vítková, G., and Kutsch, W.: The Integrated Carbon Observation System in Europe, Bulletin of the American Meteorological Society, 103(3), E855-E872, https://doi.org/10.1175/BAMS-D-19-0364.1, 2022.

Hersbach, H., Bell, B., Berrisford, P., Hirahara, S., Horányi, A., Muñoz-Sabater, J., Nicolas, J., Peubey, C., Radu, R., Schepers, D., Simmons, A., Soci, C., Abdalla, S., Abellan, X., Balsamo, G., Bechtold, P., Biavati, G., Bidlot, J., Bonavita, M., De Chiara, G., Dahlgren, P., Dee, D., Diamantakis, M., Dragani, R., Flemming, J., Forbes, R., Fuentes, M., Geer, A., Haimberger, L., Healy, S., Hogan, R. J., Hólm, E., Janisková, M., Keeley, S., Laloyaux, P., Lopez, P., Lupu, C., Radnoti, G., de Rosnay, P., Rozum, I., Vamborg, F., Villaume, S., and Thépaut, J.-N.: The ERA5 global reanalysis, Q J R Meteorol Soc., 146, 1999–2049, https://doi.org/10.1002/qj.3803, 2020.

Janssens-Maenhout, G., Crippa, M., Guizzardi, D., Muntean, M., Schaaf, E., Dentener, F., Bergamaschi, P., Pagliari, V., Olivier, J. G. J., Peters, J. A. H. W., van Aardenne, J. A., Monni, S., Doering, U., Petrescu, A. M. R., Solazzo, E., and Oreggioni, G. D.: EDGAR v4.3.2 Global Atlas of the three major greenhouse gas emissions for the period 1970–2012, Earth Syst. Sci. Data, 11, 959–1002, https://doi.org/10.5194/essd-11-959-2019, 2019.

Jiang, F., Chen, J. M., Zhou, L., Ju, W., Zhang, H., Machida, T., Ciais, P., Peters, W., Wang, H., Chen, B., Liu, L., Zhang, C., Matsueda, H., and Sawa, Y.: A comprehensive estimate of recent carbon sinks in China using both top-down and bottom-up approaches, Sci. Rep. 6, 22130, https://doi.org/10.1038/srep22130, 2016.

Jones, M. W., Andrew, R. M., Peters, G. P., Janssens-Maenhout, G., De-Gol, A. J., Dou, X., Liu, Z., Ciais, P., Patra, P. K., Chevallier, F., and Le Quéré, C.: Gridded fossil CO_2 emissions and related O_2 combustion consistent with national inventories 1959-2020 (GCP-GridFEDv2021.2) [Data set], https://doi.org/10.5281/zenodo.5565199, 2021.

Kountouris, P., Gerbig, C., Rödenbeck, C., Karstens, U., Koch, T. F., and Heimann, M.: Technical Note: Atmospheric CO_2 inversions on the mesoscale using data-driven prior uncertainties: methodology and system evaluation, Atmos. Chem. Phys., 18, 3027–3045, https://doi.org/10.5194/acp-18-3027-2018, 2018.

Kuenen, J. J. P., Visschedijk, A. J. H., Jozwicka, M., and Denier van der Gon, H. A. C.: TNO-MACC_II emission inventory; a multi-year (2003–2009) consistent high-resolution European emission inventory for air quality modelling, Atmos. Chem. Phys., 14, 10963–10976, https://doi.org/10.5194/acp-14-10963-2014, 2014.

Levin, I., Kromer, B., Schmidt, M., and Sartorius, H.: A novel approach for independent budgeting of fossil fuel CO_2 over Europe by $^{14}CO_2$ observations, Geophys. Res. Lett., 30 (23), 2194, https://doi.org/10.1029/2003GL018477, 2003.

Levin, I. and Karstens, U.: Inferring high-resolution fossil fuel CO_2 records at continental sites from combined $^{14}CO_2$ and CO observations, Tellus B, 59, 245-250. https://doi.org/10.1111/j.1600-0889.2006.00244.x, 2007.

Levin, I., Hammer, S., Eichelmann, E., and Vogel, F.: Verification of greenhouse gas emission reductions: The prospect of atmospheric monitoring in polluted areas, Phil. Trans. R. Soc. A, 369, 1906-1924, https://doi.org/10.1098/rsta.2010.0249, 2011.

Lin, J. C., Gerbig, C., Wofsy, S. C., Andrews, A. E., Daube, B. C., Davis, K. J., and Grainger, C. A.: A near-field tool for simulating the upstream influence of atmospheric observations: The Stochastic Time-Inverted Lagrangian Transport (STILT) model, J. Geophys. Res., 108, 4493, https://doi.org/10.1029/2002JD003161, 2003.

Liu, J., Baskaran, L., Bowman, K., Schimel, D., Bloom, A. A., Parazoo, N. C., Oda, T., Carroll, D., Menemenlis, D., Joiner, J., Commane, R., Daube, B., Gatti, L. V., McKain, K., Miller, J., Stephens, B. B., Sweeney, C., and Wofsy, S.: Carbon Monitoring System Flux Net Biosphere Exchange 2020 (CMS-Flux NBE 2020), Earth Syst. Sci. Data, 13, 299–330, https://doi.org/10.5194/essd-13-299-2021, 2021.

Maier, F., Gerbig, C., Levin, I., Super, I., Marshall, J., and Hammer, S.: Effects of point source emission heights in WRF–STILT: a step towards exploiting nocturnal observations in models, Geosci. Model Dev., 15, 5391–5406, https://doi.org/10.5194/gmd-15-5391-2022, 2022.

Maier, F. M., Levin, I., Conil, S., Gachkivskyi, M., Denier van der Gon, H., and Hammer, S.: Uncertainty of continuous ΔCO-based ΔffCO2 estimates derived from 14C flask and bottom-up ΔCO / ΔffCO2 ratios, EGUsphere [preprint], https://doi.org/10.5194/egusphere-2023-1237, 2023a.

Maier, F., Levin, I., Gachkivskyi, M., Rödenbeck, C., and Hammer, S.: Estimating regional fossil-fuel CO_2 concentrations from $^{14}CO_2$ observations: Challenges and uncertainties, Phil. Trans. R. Soc. A. **381**, https://doi.org/10.1098/rsta.2022.0203-, 2023b.

Maier, F., Levin, I., Hammer, S., Conil, S., Preunkert, S.: ^{14}C-based $\Delta ffCO_2$ estimates for Heidelberg and OPE and input data for the Rhine Valley $ffCO_2$ inversion (2019-2020) [Data set], https://doi.org/10.11588/data/GRSSBN, 2023c.

Monteil, G., Broquet, G., Scholze, M., Lang, M., Karstens, U., Gerbig, C., Koch, F.-T., Smith, N. E., Thompson, R. L., Luijkx, I. T., White, E., Meesters, A., Ciais, P., Ganesan, A. L., Manning, A., Mischurow, M., Peters, W., Peylin, P., Tarniewicz, J., Rigby, M., Rödenbeck, C., Vermeulen, A., and Walton, E. M.: The regional European atmospheric transport inversion comparison, EUROCOM: first results on European-wide terrestrial carbon fluxes for the period 2006–2015, Atmos. Chem. Phys., 20, 12063–12091, https://doi.org/10.5194/acp-20-12063-2020, 2020.

Nakanishi, M. and Niino, H.: Development of an improved turbulence closure model for the atmospheric boundary layer, Journal of the Meteorological Society of Japan. Ser. II, 87, 895-912, 2009.

Munassar, S., Rödenbeck, C., Koch, F.-T., Totsche, K. U., Gałkowski, M., Walther, S., and Gerbig, C.: Net ecosystem exchange (NEE) estimates 2006–2019 over Europe from a pre-operational ensemble-inversion system, Atmos. Chem. Phys., 22, 7875–7892, https://doi.org/10.5194/acp-22-7875-2022, 2022.

Munassar, S., Monteil, G., Scholze, M., Karstens, U., Rödenbeck, C., Koch, F.-T., Totsche, K. U., and Gerbig, C.: Why do inverse models disagree? A case study with two European CO_2 inversions, Atmos. Chem. Phys., 23, 2813–2828, https://doi.org/10.5194/acp-23-2813-2023, 2023.

Nehrkorn, T., Eluszkiewicz, J., Wofsy, S. C., Lin, J. C., Gerbig, C., Longo, M., Freitas, S.: Coupled weather research and forecasting–stochastic time-inverted lagrangian transport (WRF–STILT) model. Meteorol. Atmos. Phys. 107, 51–64, https://doi.org/10.1007/s00703-010-0068-x, 2010.

Newsam, G. N. and Enting, I. G.: Inverse problems in atmospheric constituent studies: I. Determination of surface sources under a diffusive transport approximation, Inverse Problems, 4, 1037–1054, 1988.

Peylin, P., Law, R. M., Gurney, K. R., Chevallier, F., Jacobson, A. R., Maki, T., Niwa, Y., Patra, P. K., Peters, W., Rayner, P. J., Rödenbeck, C., van der Laan-Luijkx, I. T., and Zhang, X.: Global atmospheric carbon budget: results from an ensemble of atmospheric CO_2 inversions, Biogeosciences, 10, 6699–6720, https://doi.org/10.5194/bg-10-6699-2013, 2013.

Rödenbeck, C., Houweling, S., Gloor, M., and Heimann, M.: CO_2 flux history 1982–2001 inferred from atmospheric data using a global inversion of atmospheric transport, Atmos. Chem. Phys., 3, 1919–1964, https://doi.org/10.5194/acp-3-1919-2003, 2003.

Rödenbeck, C.: Estimating CO_2 sources and sinks from atmospheric mixing ratio measurements using a global inversion of atmospheric transport, Tech. Rep. 6, Max Planck Institute for Biogeochemistry, Jena, Germany, 2005.

Rödenbeck, C., Gerbig, C., Trusilova, K., and Heimann, M.: A two-step scheme for high-resolution regional atmospheric trace gas inversions based on independent models, Atmos. Chem. Phys., 9, 5331–5342, https://doi.org/10.5194/acp-9-5331-2009, 2009.

Rödenbeck, C., Zaehle, S., Keeling, R., and Heimann, M.: How does the terrestrial carbon exchange respond to interannual climatic variations? A quantification based on atmospheric CO_2 data, Biogeosciences, 15, 1–18, https://doi.org/10.5194/bg-15-1-2018, 2018.

Shiga, Y. P., Michalak, A. M., Gourdji, S. M., Mueller, K. L., and Yadav, V.: Detecting fossil fuel emissions patterns from subcontinental regions using North American in situ CO_2 measurements, Geophys. Res. Lett., 41, 4381–4388, https://doi.org/10.1002/2014GL059684, 2014.

Skamarock, W. C., Klemp, J. B., Dudhia, J., Gill, D. O., Barker, D. M., Wang, W., and Powers, J. G.: A description of the Advanced Research WRF version 3, NCAR Technical note-475+STR, 2008.

Suess, H.: Radiocarbon Concentration in Modern Wood, Science, 122, 415-417, https://doi.org/10.1126/science.122.3166.415.b, 1955.

Super, I., Dellaert, S. N. C., Visschedijk, A. J. H., and Denier van der Gon, H. A. C.: Uncertainty analysis of a European high-resolution emission inventory of CO_2 and CO to support inverse modelling and network design, Atmos. Chem. Phys., 20, 1795–1816, https://doi.org/10.5194/acp-20-1795-2020, 2020.

985 Turnbull, J. C., Miller, J. B., Lehman, S. J., Tans, P. P., Sparks, R. J., and Southon, J.: Comparison of $^{14}CO_2$, CO, and SF_6 as tracers for recently added fossil fuel CO_2 in the atmosphere and implications for biological CO_2 exchange, Geophys. Res. Lett., 33, L01817, https://doi.org/10.1029/2005GL024213, 2006.

Van Der Laan, S., Karstens, U., Neubert, R. E. M., Van Der Laan-Luijkx, I. T., and Meijer, H. A. J.: Observation-based
990 estimates of fossil fuel-derived CO_2 emissions in the Netherlands using $\Delta^{14}C$, CO and ^{222}Radon, Tellus B: Chemical and Physical Meteorology, 62,5, 389-402, https://doi.org/10.1111/j.1600-0889.2010.00493.x, 2010.

Vogel, F., Hammer, S., Steinhof, A., Kromer, B., and Levin, I.: Implication of weekly and diurnal ^{14}C calibration on hourly estimates of CO-based fossil fuel CO_2 at a moderately polluted site in southwestern Germany, Tellus B: Chemical and Physical
995 Meteorology, 62, 5, 512-520, https://doi.org/10.1111/j.1600-0889.2010.00477.x, 2010.

Wang, Y., Broquet, G., Ciais, P., Chevallier, F., Vogel, F., Wu, L., Yin, Y., Wang, R., and Tao, S.: Potential of European $^{14}CO_2$ observation network to estimate the fossil fuel CO_2 emissions via atmospheric inversions, Atmos. Chem. Phys., 18, 4229–4250, https://doi.org/10.5194/acp-18-4229-2018, 2018.